AN INVESTIGATION OF TITANIUM-CARBIDE TYPE HARDFACING ALLOYS

by

Jorge C. Lira

ProQuest Number: 10782528

ProQuest 10782528

T-2826

A thesis submitted to the Faculty and the Board of
Trustees of the Colorado School of Mines in partial
fulfillment of the requirements for the degree of Master of
Science (Metallurgical Engineering).

Golden, Colorado

Date ___9/12/83___

Signed: _____
Jorge C. Lira

Approved: _____
Robert H. Frost,
Thesis Advisor

Golden, Colorado

Date ___9/12/83___

_____
William D. Copeland
Department Head
Metallurgical Engineering

ii

ABSTRACT

An evaluation or titanium-carbide type hardfacing alloys was done in two experimental studies. In the first, a commercial alloy was deposited using a wide range of welding process variables to determine the effects of these variables on microstructure and low-stress abrasion resistance. In the second study, alloy composition was varied to determine the effects of microstructural variables on low-stress abrasion resistance. It was found that dilution did not significantly affect the volume fraction of titanium carbides in the deposit, and thus similar wear rates were observed over the whole range of process variables studied. On the other hand, significantly different wear rates were observed with two types of alloy matrices tested. An austenitic/martensitic matrix yielded a low wear rate, which was attributed to the sliding of the abrasive on the carbides. A ferritic matrix yielded a higher wear rate, which was explained by the carbides being easily pulled out from the matrix during the abrasion process. With a constant matrix material, the dry sand/rubber wheel test used was not able to show any discernible differences in abrasion resistance between various carbide volume fractions and distributions, probably

due to the very fine scale of the carbide distribution.

TABLE OF CONTENTS

LIST OF FIGURES

LIST OF TABLES

ACKNOWLEDGEMENTS

1 INTRODUCTION

Material loss caused by wear is responsible for a large fraction of the operating costs of ground engaging equipment used in the mining, agricultural and earth-moving industries. Abrasion consists of the scratching, cutting and gouging action of hard particles on the surface being abraded, and it accounts for about 50 percent of wear losses. Hardfacing by arc welding or other processes involves the application of an abrasion resistant metal layer over a usually softer metal part, and it offers an effective means of reducing abrasive wear (1-10).

1.1 HARDFACING PROCESSES AND ALLOY SYSTEMS.-

Hardfacing consumables can be applied to a metal surface by almost any type of welding process. Usually processes are favored which provide a relatively high deposition rate and ease of application. A relatively smooth bead contour may be desirable under certain circumstances because hardfacing deposits are very difficult to machine. The specific process used depends on the nature of the consumable, the base metal, the section thickness,

and the amount of dilution desired for the specific application. Table 1 is a summary of the processes available.

Several alloy systems are used for hardfacing, and their proper selection depends on the specific application being sought. In the case of abrasive wear, the correct alloy must be chosen to suit the particular tribological system, which consists of the base material, the surfacing material, the abrasive agent, and the environment. In fact, when dealing with wear control, each situation is unique and a systems approach must be used, in which all of the elements are considered. Table 2 provides information on the properties and applications of the important types of hardfacing alloys. Of these, the tungsten-carbide composites and the high-chromium white irons offer the highest abrasion resistance. The latter are more widely used because of their low cost and good resistance to scratching-type abrasion in which relatively low impact is involved. Both types of alloys feature a hard second phase dispersed in a relatively softer matrix. Experience and research (11,12) have shown that the optimum microstructure for abrasion-resistant castings and weld overlays consists of a composite structure in which the hard phase is harder

Table 1

Summary of Available Hardfacing Methods (3)

Arc Welding

Shielded Metal Arc
Flux Cored Arc
Submerged Arc
Gas Tungsten Arc
Plasma Arc
Electroslag Welding

Oxyfuel Gas

Oxyacetylene Welding

Thermal Spraying

Flame Spraying
Plasma Spraying
Electric Arc Spraying
Detonation Gun Process

Table 2

Properties and Applications of the Most Important Types of Hardfacing Alloys (3).

General Alloy Type	Typical Deposit Chemistry	Identification	Characteristics	Applications
Low Carbon Steel Buildup	0.1% C, 1% Mn, 0.5% Si. 0.8% Cr 0.5% Ni, bal. Fe	AWS—none Trade Names: Buildup, BU, Multipass, etc.	Ferritic, 20-35 HRC, machinable, magnetic, tough, some strength, ductile, buildup to unlimited thickness	Rebuild mild steel parts, mine car wheels, shafts, gears, rolls, cams, trunnions
Manganese Steel Buildup	1.1% C, 14% Mn, 1% Ni, 0.5% Mo, 2% Cr, 0.5% Si, bal. Fe—also high Cr modifications	AWS—A5.13 FeMn—A + B Trade Names: Mangjet, NiMn, Nicromang, Ranmang, etc.	Austenitic, 90 RB, workharden to 45 RB, tough, ductile, non-magnetic exceptional impact resistance, fair abrasion resistance	Rebuild Mn Steel castings, crusher rolls, railway switchgear, breaker bars, hammermill hammers
Martensitic Steel Hardfacing	0.5% C, 1% Mn, 0.5% Si, 5% Cr, 1.5% Mo, bal. Fe	AWS—none Trade Names: Self Hardening, Hardalloy 58, Methard 4, etc.	Martensitic, 45 to 60 HRC, strong to 500 C (900 F), resist galling, fair abrasion resistance, moderate impact toughness and ductility	Nonlubricated undercarriage parts of tractors, cable sheaves, crane wheels, pipe forming rolls
Chromium-Iron Hardfacing	4% C, 20% Cr, 2% Mn, 1% Si, 1% Mo, 0.5% Ni, bal. Fe	AWS—A5.13 FeCr—A1 Trade Names: Stoody 100 HC, S.A. Superchrome, Delcrome 91, etc.	Cr₇C in Martensite-retained austenite, 45 to 60 HRC, usually cracked as deposited, limit 2-4 layers, excellent abrasion resistance up to 500 C (900 F)	Dipper teeth, pulverizers, scoop tram buckets, drag chains, pusner shoes, hammermill hammers, slusher edges
Copper-Base Hardfacing	10% Al, 1.5% Fe, 0.3% Sn, bal. Cu	AWS—A5.13 CuAl-A to E, etc. Trade Names: Ampcotrode 10, Sodel 36, etc.	Low friction with steel, resist metal-to-metal wear and seizure, corrosion resistant, machinable, unlimited thickness	Gears, bearings, shafts, die molds, hydraulic pistons, buildup of copper-base castings
Tungsten Carbide Hardfacing	60% WC bal. mild steel	AWS—A5.13 WC—20/30, etc. Trade Names: Borium, Tungsite, Rantung, etc.	Undissolved WC in tool steel matrix, usually cracks as deposited, excellent abrasion resistance, oxidizes, >400 C (750F), limited to one layer	Rock drills, earth augers, cutter teeth, drill collars, implements to cut silica
Cobalt-and Nickel-Base Hardfacing	28% Cr, 5% W, 1% C, bal. Co—also nickel-base alternatives	AWS—A5.13 CoCr—A to C Trade Names: Stellite, Cobend Hardface #6, etc.	Carbides in alloy matrix, 40-55 HRC, good hot hardness to 800 C (1500 F), polish in service, resist heat, corrosion, hot metal-to-metal wear, erosion, cavitation & impact	Knives, roasting oven flows, tongs for handling hot castings, hot forming and extrusion dies

than the abrasive particles, and in which the matrix phase
is strong enough to hold the second-phase particles in
place. This is discussed in the following section.

1.2 ABRASION AND ABRASION RESISTANCE

1.2.1 Definition

Abrasive wear can be defined in different ways. A good
definition is that given by the Australian Welding Research
Association (6): "Abrasion involves the forced indentation
of hard particles across a surface, which then exhibits
scratches or grooves. Removal of the material depends on
the ability of the abrasive particles to indent or penetrate
the surface". The particles may be anywhere from soil to
crushed mineral to metallic debris, depending on the
situation.

1.2.2 Types of Abrasive Wear

Based on what approach is taken, there are different
ways to classify abrasive wear. "Two-body abrasion" refers
to wear caused by abrasive sliding on a material, and
"three-body abrasion" refers to wear caused by abrasives

trapped between two moving surfaces. On the other hand,
Richardson (13,14) differentiated between wear caused by an
abrasive of hardness equal to or less than that of the wear
surface (a "soft abrasive") and that caused by an abrasive
harder than the worn surface (a "hard abrasive").

The most common classification in the United States is
based on the observed wear damage (15):

Gouging Abrasion.- Results in the removal of large
particles from a metal surface. Worn surfaces show heavy
gouges.

High-Stress Grinding Abrasion.- Occurs during the
progressive fragmentation or grinding of the abrasive which
was initially of small size and takes place on the surfaces
employed to grind the abrasive. The wear is believed to be
caused by concentrated compressive stress at the point of
abrasive contact and to result from plastic flowing and
fatiguing of ductile constituents and cracking of hard
constituents of the metal surface. The use of the words
"high stress" in this classification is intended to imply
that the crushing strength of the abrasive is exceeded. An
example of high-stress grinding abrasion is the wear

experienced by the steel balls in a ball mill.

Low-Stress Scratching Abrasion or Erosion.- The result of this type of abrasive wear is scratching of the metal surface, and the scratches are usually minute. The stress imposed on the abrasive particle does not exceed the crushing strength of the abrasive. This is usually "two-body" abrasion, like that experienced by agricultural equipment, or digger teeth.

1.2.3 Mechanism of Material Removal in Low-Stress Abrasion

Many gross simplifications are necessary if one attempts to model the process of abrasive wear. Usually more than one mechanism is present in any one situation due to the non-homogeneity of the conditions. For example, the abrasive particles will probably differ in size, shape, and hardness, and in the micro-scale various mechanisms of removal will act simultaneously. However, there are two extreme mechanisms of material removal that can be differentiated: one includes plastic deformation and the other involves fracture as the dominant effect. These are described comprehensively by Moore (11).

Where plastic deformation is the rate controlling step, first the particles form grooves in the metal surface by displacing metal to the sides of the grooves. Ultimately, the sides of the grooves become detached by fracture and become part of the wear debris. A simplified treatment of this mechanism yields a wear rate of the form:

$$W = K_1 K_2 K_3 (\sigma/H) \; ; \qquad (1)$$

where W is the volume wear per unit area per unit sliding distance, σ is the applied load per unit area, H is the hardness of the surface, K_1 is the summed probability of wear debris formation, K_2 is the mean proportion of groove volume removed when debris formation occurs, and K_3 is related to the shape of the particle. As can be seen, obtaining values for K_1, K_2, and K_3 is non-trivial, and even then the equation is an oversimplification of what really goes on. For example, it does not take into account the effects of strain hardening, which has been found to be very important in determining the the wear rate (16). Avery showed that surface work hardening is the mechanism responsible for the performance of austenitic steels and irons in abrasive media.

For materials with lower fracture toughness, the indention of abrasive particles into the the surface may cause cracks to form normal to the surface and laterally extending from beneath the indention towards the surface. Cracking is in this case the primary mechanism for material removal, and would be expected to be a function of fracture toughness as well as the load and the hardness. The wear rate can be described by the following equation (11):

$$W = k_5 \frac{\sigma^{5/4} d^{1/2}}{K_C^{3/4} H^{1/2}} \; ; \qquad\qquad (2)$$

where d is the mean particle diameter, Kc is the fracture toughness of the material and k_5 is a constant dependent on particle shape and distribution. In theory, the rate of material removal by the fracture mechanism should be much higher than that from the plastic flow mechanism; however, real situations encompass both mechanisms and seldom can be described with any type of acceptable model.

1.2.4 Factors Affecting Abrasion Resistance

Figure 1 is a schematic of the major variables which control abrasion resistance of an alloy. As shown, the
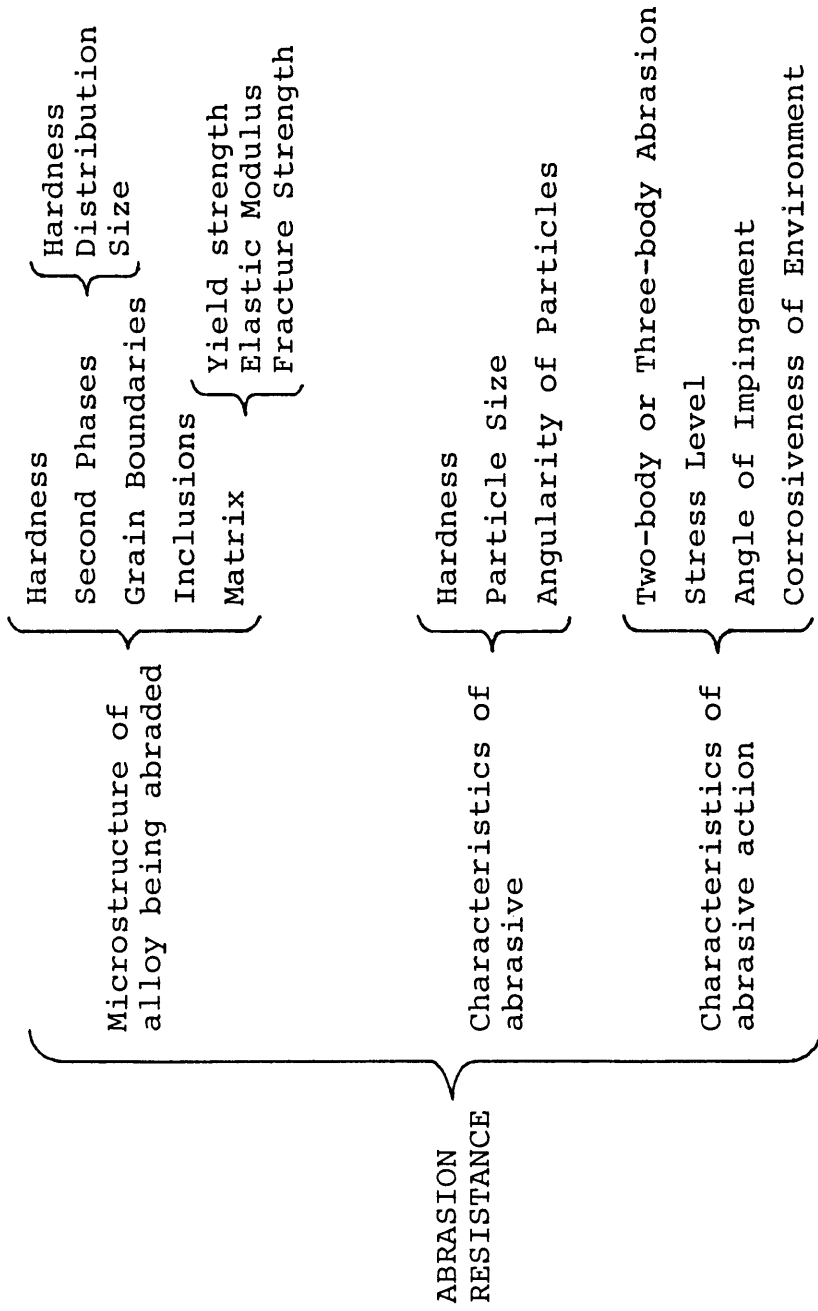
Figure 1.- Major variables which control abrasion resistance.

variables may be broken down into three major groups, all of which must be considered when trying to combat abrasive wear in a given situation. The numerous variables involved make it very difficult to quantitatively establish meaningful relationships between the variables themselves. Thus, the treatment of abrasive wear has progressed very little as a science, even though it has been a major concern for many decades. Most of the knowledge on how to reduce abrasive wear has been gathered from years of empirical experience and various kinds of testing under varying conditions.

Testing for abrasive resistance poses its own problems. As discussed by Avery (17), the requirements for a good laboratory test would be: (1) reproducibility or reliability, (2) ranking ability and, (3) validation by correlation with service. While (1) and (2) may be met by various methods, the third requirement is the hardest to meet because of the variety of actual service conditions that are so far removed from laboratory test conditions. Presently, only one abrasion test exists as an American Society of Testing Materials (ASTM) standard, which is the G-65-80 dry sand/rubber wheel test (18), good only for low-stress scratching abrasion. Its correlation with actual service conditions has been described as good (19) although

its results should be used carefully and not freely
extrapolated to large scale situations.

1.3 METALLURGICAL CONSIDERATIONS

As explained in Figure 1, abrasion resistance is
influenced by alloy microstructure, abrasive
characteristics, and the nature of the abrasion process. In
combatting abrasion, the metallurgists job is usually
limited to the control of alloy microstructure since the
other two main factors are usually fixed and determined by
the kind of environment present and the service required by
the particular part or component. This is where the proper
selection of hardfacing alloy comes into play: it is the
alloy microstructure that will control abrasion resistance
if everything else is held constant.

1.3.1 Microstructural Effects

There is no microstructure that will be optimum for
every abrasive condition. According to Zum-Gahr (12), the
following parameters are all important to wear rate:

- Inclusions
- Second phases

- Grain boundaries

- Matrix structure

- Internal notches

- Anisotropy

For hardfacing alloys, the wear rate is controlled mainly by second phases present and by the nature of the matrix. Hard second phases are very effective in increasing the abrasion resistance of hardfacing alloys. Making a hardfacing alloy very hard is impractical because this property is usually associated with very low toughness, which would make the weld deposit spall off easily. Thus the best way to take advantage of a high-hardness phase for abrasion resistance is by using an appropriate distribution of second phase particles in a relativly softer matrix phase. The matrix will then control the bulk properties while holding on to the hard phase, which will control the wear rate.

The most common second phase used in commercial hardfacing alloys are carbides, because of their high hardness and thermodynamic stability. Table 3 shows that the hardest phases in metallic systems are carbides. For example, $(Fe,Cr)_7C_3$ carbides are responsible for most of the abrasion resistance of high chromium white irons. The

Table 3

Hardness of Various Minerals and Alloy Phases (20)

Mineral	Hardness Knoop*	HV
Talc	20	
Carbon	35	
Gypsum	40	36
Calcite	130	140
Fluorite	175	190
Apatite	335	540
Glass	455	500
Feldspar	550	600 to 750
Magnetite	575	
Orthoclase	620	
Flint	820	950
Quartz	840	900 to 1280
Topaz	1330	1430
Garnet	1360	
Emery	1400	
Corundum	2020	1800
Silicon carbide	2585	2600
Diamond	7575	10000

Material or Phase	Hardness Knoop*	HV
Ferrite	235	70 to 200
Pearlite, unalloyed		250 to 320
Pearlite, alloyed		300 to 460
Austenite, 12% Mn	305	170 to 230
Austenite, low alloy		250 to 350
Austenite, high Cr iron		300 to 600
Martensite	500 to 800	500 to 1010
Cementite	1025	840 to 1100
Chromium carbide $(Fe,Cr)_7C_3$	1735	1200 to 1600
Molybdenum carbide Mo_2C	1800	1500
Tungsten carbide WC	1800	2400
Vanadium carbide VC	2660	2800
Titanium carbide TiC	2470	3200
Boron carbide B_4C	2800	3700

influence of carbides on abrasion resistance depends on
their hardness relative to the hardness of both the matrix
and the abrasive. Naturally, the carbides have to be harder
than the abrasive to be effective in reducing wear, but
other factors must be considered.

If hard carbides are embedded in a soft matrix, wear
resistance should increase with decreasing mean free path (λ)
between carbides, because preferential matrix removal gets
more difficult. Moreover, carbide pullout is relatively
easy with a soft matrix, so the only way to reduce this
problem is by placing the carbides very close to each other.
Studies have shown that, for a given volume fraction of
carbides, the wear rate increases as $\lambda^{1/2}$(11,12).

If the carbide hardness is similar to that of the
matrix, the carbides may act as internal notches and
actually reduce the wear resistance by starting microcracks
close to the surface, where the stress is the highest. For
example this may happen with M_3C carbides embedded in a
martensitic matrix in tool steels.

1.3.2 Hardfacing Alloys

In hardfacing alloys, carbides or any other second phase may be introduced in the final weld deposit by two methods:

(i) the alloy chemistry can be adjusted so that the carbides precipitate during solidification of the deposit by some metallurgical reaction (eutectic, peritectic, etc.).

(ii) Carbides can be introduced in the solid state into the weld pool, after which the matrix solidifies around the carbides.

A common example of type (i) is given by the family of chromium white iron hardfacing alloys. These owe their abrasion resistance to $(Fe,Cr)_7C_3$ carbides distributed in the microstructure either as a primary solidification phase or as part of a $(Fe,Cr)_7C_3/\gamma$ eutectic structure. The chemistry of these alloys is chosen so that it falls near the γ/M_7C_3 eutectic valley in the Fe-Cr-C ternary system as shown in Figure 2. Primary M_7C_3 carbides are produced in alloys that cool in the hypereutectic side. Alloys with lower carbon and chromium contents will solidify on the hypoeutectic side forming austenite as the primary phase, and all of the carbides will be from the M_7C_3/γ eutectic
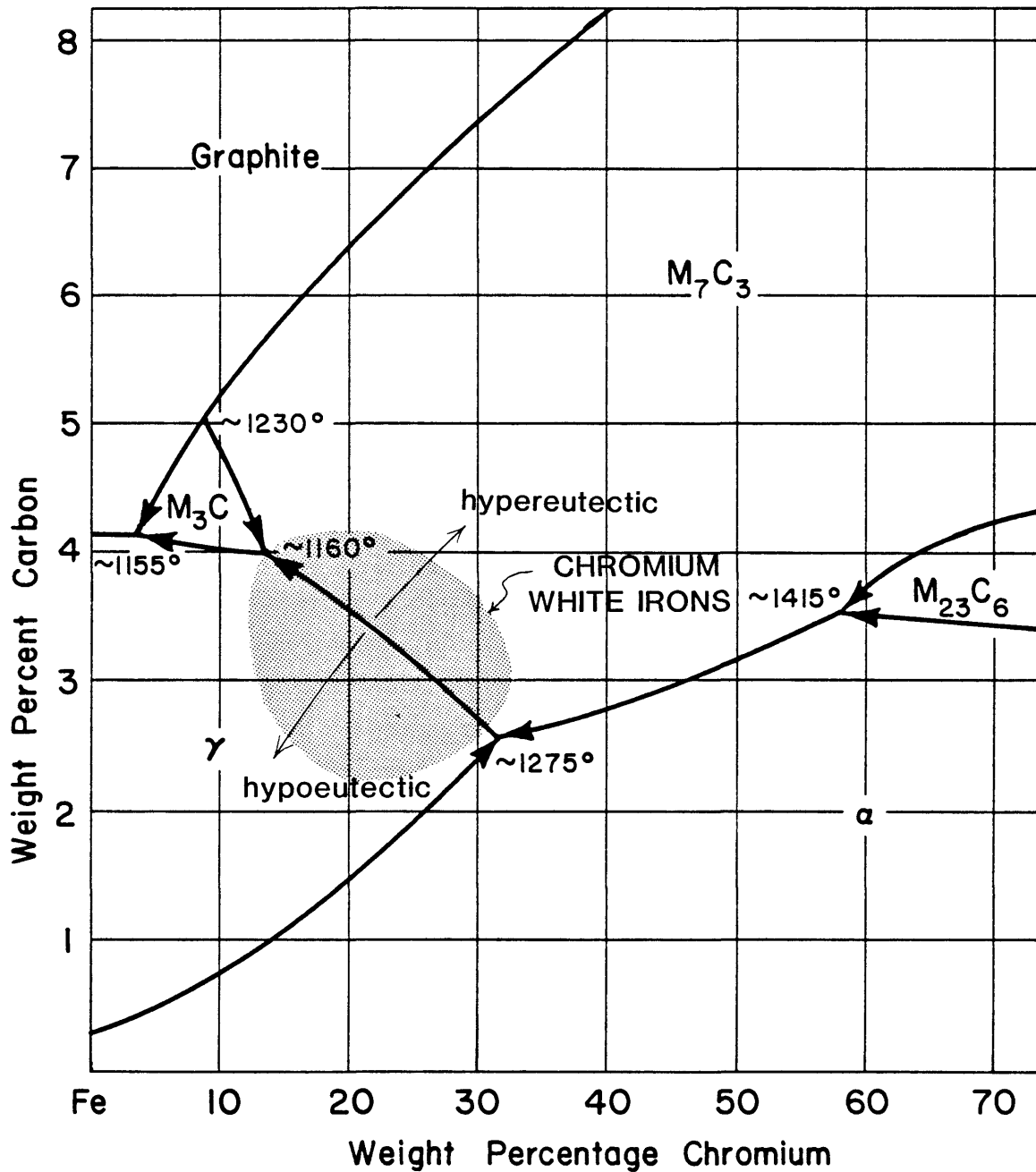
Figure 2.- Portion of the liquidus projection of the
Fe-Cr-C ternary system showing the approximate
composition range for chromium white irons.
After (21).

that forms between the Y dendrites.

Alloys of type (ii) are restricted to carbides which are stable enough at high temperatures so they will not dissolve in the molten weld pool. Common examples are tungsten carbide in a cobalt matrix or titanium carbides in a ferrous matrix. There are several methods by which the carbides may be placed in the weld pool; the selection of the process depends on the desired deposition rate, dilution, and ease of process control. The most popular methods include: (a) powder spraying; (b) open-arc surfacing using a tubular electrode; and (c) oxyacetylene welding using a tubular electrode. Even though higher deposition rates are obtained by the first two methods, oxyacetylene surfacing is still used where it is critical to achieve low dilution and heat input (22). More recently, a plasma-arc hardfacing process has been successfully used to deposit powdered mixtures containing the carbides of Ti, V, Zr, Nb and W (23). These overlays have been shown to provide excellent wear resistance (23,24).

The main metallurgical difference between alloy types (i) and (ii) involves control of the size, volume fraction and distribution of the hard phase. Formation of the hard

phase in type (i) alloys depends on the chemical composition
and cooling rate of the weld pool, which will dictate the
solidification conditions. In type (ii) alloys, the
introduction of the hard phase is independent of
solidification conditions, and therefore the local chemistry
should only affect the solidification sequence of the matrix
around the carbides. This of course will only be true if
there is little or no dissolution of the carbides into the
matrix during the welding thermal cycle.

1.4 ABRASION-RESISTANT ALLOYS BASED ON TITANIUM CARBIDE

Titanium carbide is one of the hardest phases known.
Table 3 shows that its hardness exceeds that of SiO_2, WC, or
the $(Fe,Cr)_7C_3$ carbides present in the high-chromium white
irons. Titanium carbide is also one of the most
thermodynamically stable carbides as shown by the carbide
free energy diagram in Figure 3 (25). Titanium carbide
particles are stable in solution at temperatures well above
the melting points of iron and steel alloys. Thus, they can
be transferred across the arc in the solid state, and they
do not dissolve in the weld pool.

The original patent for using TiC in hardfacing
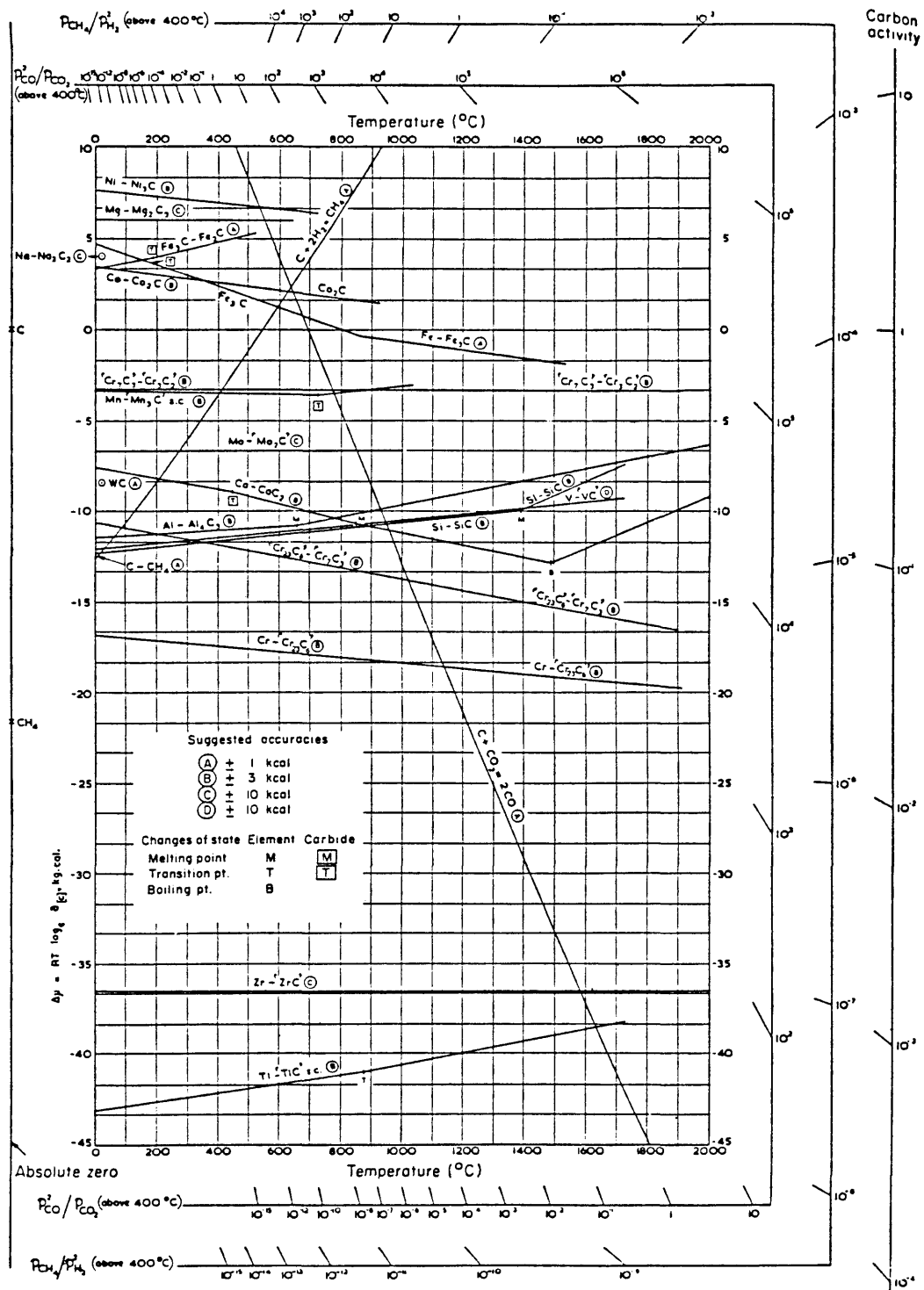
Figure 3.- Free energy of formation of various
carbides as functions of temperature(25).

overlays in 1966 (25) called for flux-cored tubular
electrodes which contained both metallic titanium and
titanium oxide powders in the flux core. A considerable
amount of graphite powder was also included with the
objective that the titanium oxide would first be reduced to
titanium, and then TiC particles would precipitate from the
melt during solidification. This process was found to work;
however, titanium losses as high as 50% were experienced,
and these losses made the process economically unattractive.

Titanium-carbide containing overlays are currently
produced using the open-arc process which utilizes TiC
particles in a flux-cored wire electrode. Welding
electrodes containing TiC powder produce hardfacing deposits
with excellent abrasion resistance, but their acceptance has
been limited because of difficulty in application. However,
as Sereda et. al. point out (27), titanium carbide appears
to offer the greatest promise as a substitute for tungsten
carbide in "hard" alloys. Its melting point, hardness and
oxidation resistance are higher than those of WC, although
it does not quite match the latter material in elastic
modulus and thermal conductivity.

Even though titanium carbides are frequently used in

powder metallurgy (28), tool coatings (29,30) and spray
powders (23,24), they are not common in castings or
hardfacing wires. The problem with castings is that
titanium carbides are so light (s.g.=4.93) that they tend to
rapidly float in a ferrous melt. This is not a problem in a
weld pool because solidification is so fast that most of the
carbides manage to stay in the weld.

There is very little information in the literature on
TiC-containing overlays, and most of it relates to
powder-spraying techniques using relatively sophisticated
equipment. The relative abundance of titanium (especially
in the form of oxide) compared to that of tungsten or
vanadium or any of the elements forming the hardest carbides
suggests a need for work on optimizing hardfacing
consumables for arc welding containing titanium carbide. As
mentioned before, consumables of this type are available but
their use is currently very limited; in fact, they do not
even appear in most classifications of hardfacing
consumables.

1.5 PURPOSE OF THIS INVESTIGATION

This study was aimed at simultaneously evaluating the

performance of TiC-based hardfacing alloys, understanding

the mechanisms by which they resist abrasive wear, and

understanding the variables involved in these mechanisms.

The investigation was divided into two parts: in the first

part a commercial TiC-based alloy (alloy A) was welded onto

1020 steel plate at systematically varied welding process

parameters using the open-arc process. The object here was

to observe how the process parameters affected the

characteristics of the deposited alloy, including its

low-stress abrasion resistance. In the second part of the

investigation, the process parameters were held fixed and

the microstructure of the alloy was changed so that the

effect of microstructural variables could be evaluated.

1.5.1 Study on Effect of Process Variables

Figure 4 is a block diagram showing how the different

variables interact in welding a hardfacing alloy. By fixing

the chemical composition, i.e., by considering any one

alloy, the characteristics of the deposit may be altered,

within certain limits, by altering variables such as

voltage, current and travel speed. The extent to which this

can be accomplished depends on the alloy system. For

example, in doing a process-parameter study on a chromium
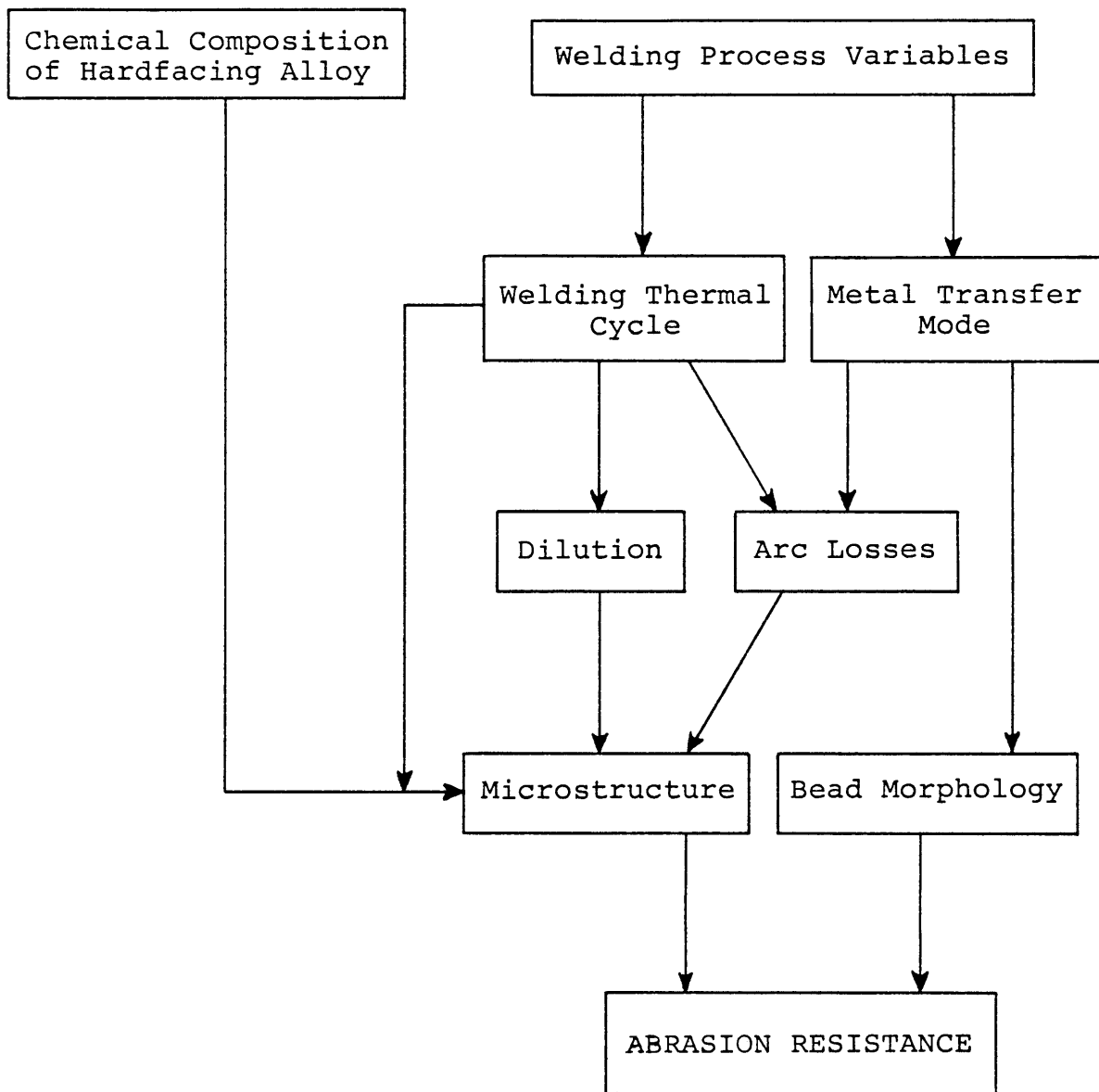
Figure 4.- Block diagram showing interaction of
            different variables when welding a
            hardfacing alloy.

white iron hardfacing alloy, Rense (31) found that the microstructure of these alloys is extremely sensitive to the amount of dilution with the base plate, which was a strong function of variables such as current, voltage, and a parameter he defined as "Deposition Ratio" which is proportional to the size of the bead. This high sensitivity follows from the location of chromium irons in the Fe-Cr-C ternary system. Relatively low levels of dilution are enough to shift a hypereutectic alloy (see Figure 2) to turn hypoeutectic, thus drastically changing the volume fraction and distribution of M_7C_3 carbides.

In TiC-based alloys the situation differs because the carbides are not produced by any metallurgical reaction but are introduced in the solid state from the core of the consumable wire. Therefore a different behavior is expected, and this was the matter of this part of the investigation.

1.5.2 Study on Effects of Microstructure

The microstructural parameters of interest in this part of the investigation were the size, volume fraction and distribution of the carbides, and the nature of the matrix

holding the carbides in place. Four additional alloys were tested for this purpose, one of which was commercially available as a flux-cored consumable, and three of which were manufactured in the laboratory using a special technique.

2 EXPERIMENTAL PROCEDURE

2.1 HARDFACING CONSUMABLES USED

To study the effects of welding process parameters on a single alloy, a commercially available flux-cored wire was used (McKay 240 TiC-O), and was labelled alloy A. Its diameter was 2.8 mm (7/64 in) and was welded onto half-inch thick 1020 steel plate. The chemical compositions of the wire and the base plate are shown in Table 4.

For the study on the effects of microstructure, four alloys were investigated, labelled 1 through 4. Alloys 1, 2 and 3 were manufactured in the laboratory with a technique described below, while alloy 4 was another commercial wire (CONARCO Tubularc 258 TiC-O), 2.4 mm (3/32 in) in diameter. Table 5 gives the nominal chemical composition of these wires.

2.1.1 Making of Wires in the Laboratory

The three experimental alloy wires were made by a process currently being studied by Jaramillo (32), which will be concisely described. For each alloy, a capsule was

Table 4

Chemical Compositions of the Base Plate and of an Undiluted Hardfacing
Deposit of Alloy A

COMPOSITION (Wt.%)

	C	Si	Mn	Mo	Cr	Ni	Cu	Ti	P
1020 steel base plate	0.22	0.21	0.50	0.07	0.04	0.07	0.16	--	0.005
Undiluted hardfacing deposit	4.60	0.10	1.65	0.06	7.20	0.04	0.02	6.40	0.005

Table 5

Nominal Chemical Composition of Hardfacing Alloys
1, 2, 3 and 4

Alloy	%Cr	%C	%Mn	%TiC	%Mo	%Fe
1	4.07	3.33	1.71	4.58	--	Balance
2	3.42	2.79	1.43	19.97	--	Balance
3	--	0.08	0.4	9.42	--	Balance
4*	7.5	1.7	--	6.9	1.7	Balance

* From weld composition, supplied by manufacturer

machined from 1008 steel 1-in rod to the dimensions shown in
Figure 5. Then, depending on the overall chemical
composition desired, a metal-powder mixture was compacted
inside the capsule until completely full, after which a lid
of 1008 steel was welded on top using the GTAW process (see
Figure 5). The powder compositions were back-calculated
starting with the desired chemical compositions of the
hardfacing deposits, assuming a 30% dilution level with the
1020 steel base plate. Details of these calculations appear
in Appendix 1. Table 6 shows details of the desired
microstructure of the experimental alloys. Alloys 1 and 2
were aimed towards a similar austenite/martensite matrix,
the difference being the volume fractions of TiC. Alloy 3
featured a ferritic matrix with absolutely no added alloy
content, except for the minor amounts already present in the
1008 steel capsule. Note from Table 5 that the desired
chromium content in alloys 1 and 2 was much leaner than
alloys A and 4. This was done for comparison reasons.

The powder mixtures were made from reagent-grade
metallic powders at about 100 mesh, except for the TiC
powder which was -165 mesh. They were compacted into the
capsules using a specially-made punch (see Figure 6) with a
compacting pressure of 10,000 psi.
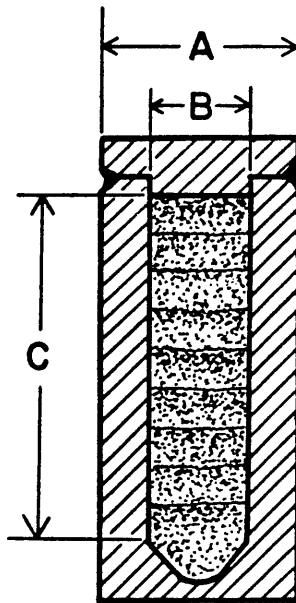
Figure 5.-   1008 steel capsule before being mechanically
             formed into wire.

Table 6

Desired Microstructures of Alloys Used in Experimental
Matrix 2

		DESIRED MICROSTRUCTURE	
ALLOY	VOLUME % TiC	MATRIX	WIRE
1	5	Austenitic/Martensitic	Experimental
2	20	Austenitic/Martensitic	Experimental
3	10	Ferritic	Experimental
4	10	Austenitic/Martensitic	Commercial
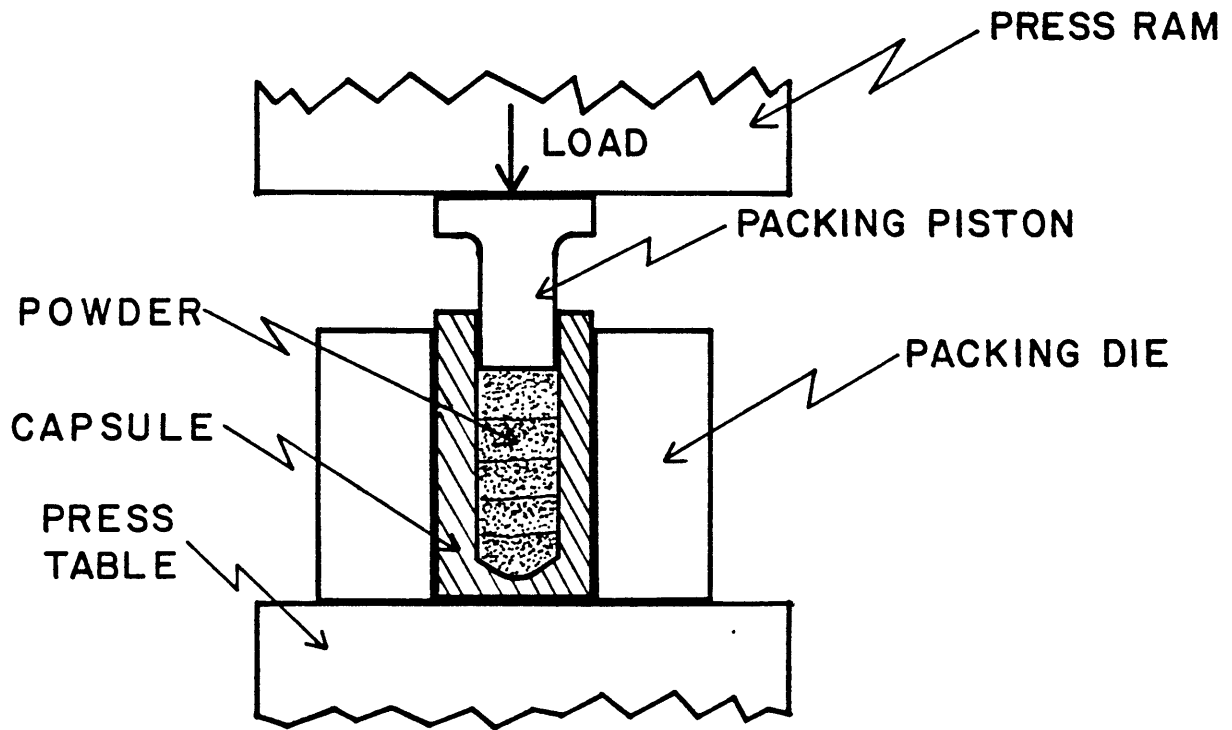
Figure 6.- Piston-and-die system used to compact powders
             into 1008 steel capsules.

Three forming stages were used to make wire from the
capsules: hot rolling, cold rolling and swaging. The final
wire diameter after swaging was 2.4 mm (3/32 in). Before
hot rolling, the capsules were preheated to about 750 C; two
intermediate anneals at the same temperature were used
during hot rolling. After swaging, each capsule yielded a
10-12 foot-long wire. All the wires were thoroughly cleaned
with methanol before welding to minimize the presence of
residual grease or oil from the forming operations.

2.2 WELDING EQUIPMENT USED

For the process-parameter part of this investigation,
automatic open-arc flux-cored welding (FCAW) was used.
However, the experimental alloys were welded with the
automatic submerged-arc process (SAW). In both cases,
Hobart gas-metal-arc automatic welding equipment was used,
including a Model AI-22 wire feeder and torch, and a model
RC500 constant potential DC power supply. Voltage and
current were measured by connecting a Hewlett-Packard HP
7100BM strip chart recorder to the power supply.

2.3 EXPERIMENTAL MATRICES

2.3.1 Matrix 1

To study the effect of changing the welding parameters on alloy A, variations of current, voltage and travel speed were needed in a systematic way so that the observed effects could be related back to these parameters. A discussion follows on the way the experimental parameters were chosen.

Arc welding involves many different process variables, some independent and some dependent. The important independent variables in the experimental setup used here were:

V = voltage setting in the machine

w = wire speed

S = travel speed

The important dependent variables are:

I = current

V = voltage

l = electrode stickout

Since the common variables one deals with are V and I, the object was to weld at different conditions by moving in

V-I process space. To eliminate all the extra variables

involved, some constraints had to be taken. The first was

to keep a constant amount of material deposited per unit

length of bead for all test samples, which was accomplished

by setting:

$$\frac{W}{S} = D = \text{constant for all welds} \qquad (3)$$

Another degree of freedom was eliminated by choosing 3

different values for heat input, given by:

$$\frac{VI}{S} = H \qquad (4)$$

These two equations defined the experimental matrix

shown in Figure 7. In this Figure, each point corresponds

to a different weld sample, and each line to welds done at a

constant heat input. The values 1, 1.5 and 2.0 MJ/m were

chosen so as to cover the widest range of conditions as

possible without exceeding the process limitations of the

welding equipment used. The value of D=6 was chosen

empirically so that at the low and high heat inputs the

conditions were within machine limitations, and so that the

bead size was maintained large enough for practical

hardfacing applications.
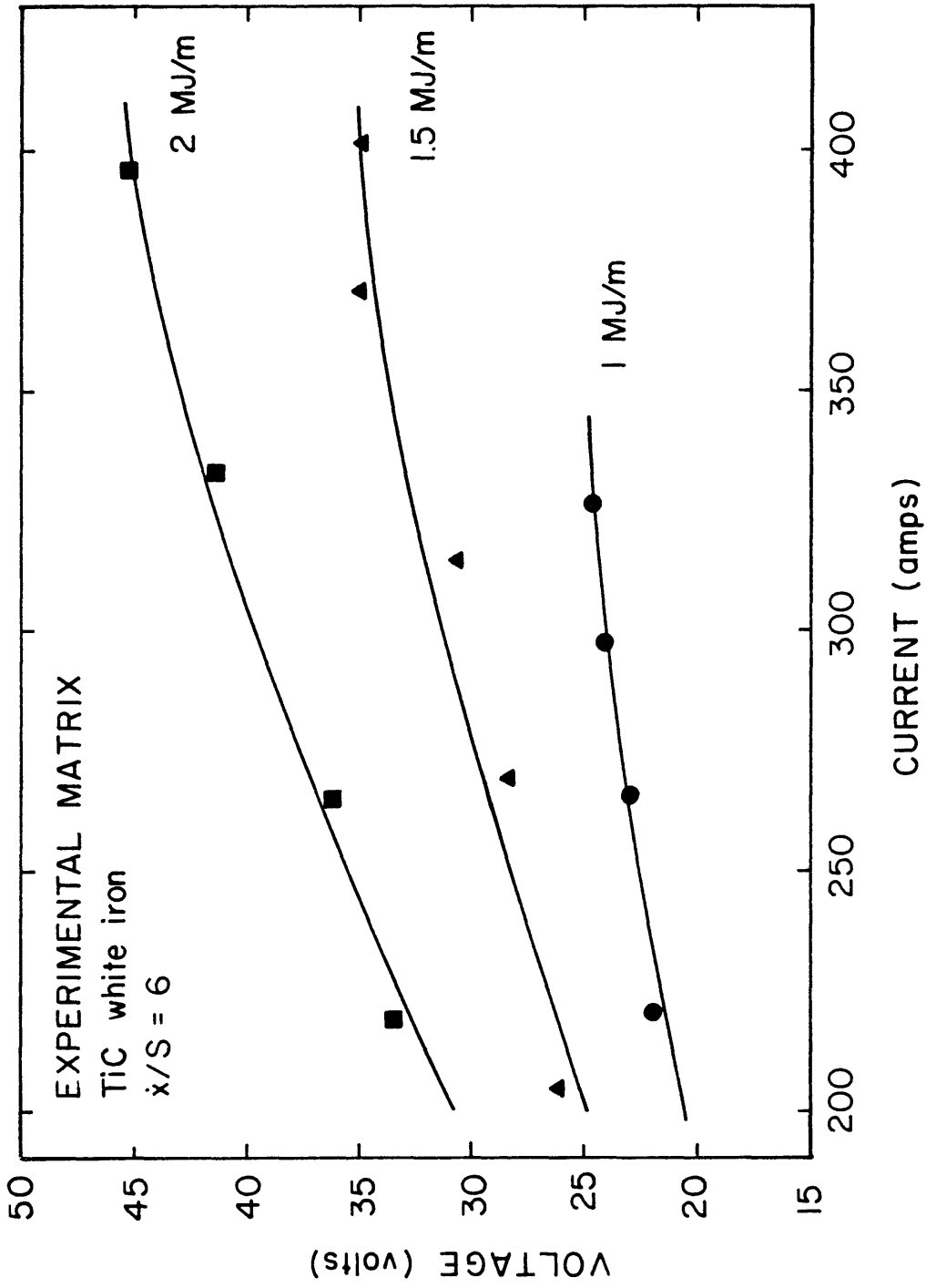
Figure 7.- Experimental matrix 1, using alloy A. Each point represents one sample.

2.3.2 Matrix 2

The second experimental matrix was based on microstructural changes. Four microstructures were studied, those of alloys 1, 2, 3 and 4, whose desired characteristics are shown in Table 6. Alloys 1, 2 and 3 were made in the laboratory as described above, and alloy 4 was a commercial wire.

2.4 WELDING PROCEDURE

2.4.1 Matrix 1

Single-layer deposits of alloy A were made on half-inch thick AISI 1020 steel plate, using the automatic flux-cored arc welding process (FCAW) with DC reverse polarity; the wire diameter was 2.8 mm (7/64 in) and the plate dimensions were 305 by 102 by 13 mm (12 by 4 by 0.5 in).

Thirteen samples were made, corresponding to each point in Figure 7. Each base plate was preheated to 200 C before the first pass, and allowed to cool to 200 C between passes, in an attempt to maintain similar heat-sink conditions every

time. Beads were laid parallel with approximately a fifty
percent overlap; enough beads were laid down to cover the
width of the plate (see Figure 8). It was found that
complete removal of the slag between passes was crucial to
avoid extreme porosity caused by slag entrapment.

Each specimen was sectioned as shown in Figure 9 and
subjected to macrostructural, microstructural and chemical
analyses, and low-stress abrasive wear testing.

2.4.2 Matrix 2

Welding of alloys 1 through 4 was also done on 1020
steel, this time 5/8 in thick. The automatic submerged-arc
process was used, being the easiest way to apply the alloys
under controlled conditions, i.e., minimizing material loss
by spatter and arc oxidation. A commercial flux was used
(Oerlikon OP 121TT); it was chosen because it showed better
slag detachability than other fluxes that were available,
even though the detachability was by no means good. All
samples were welded at about 30 volts and 350 amps.

One sample was made from each alloy, with a similar
procedure as for matrix 1. Specimens were sectioned
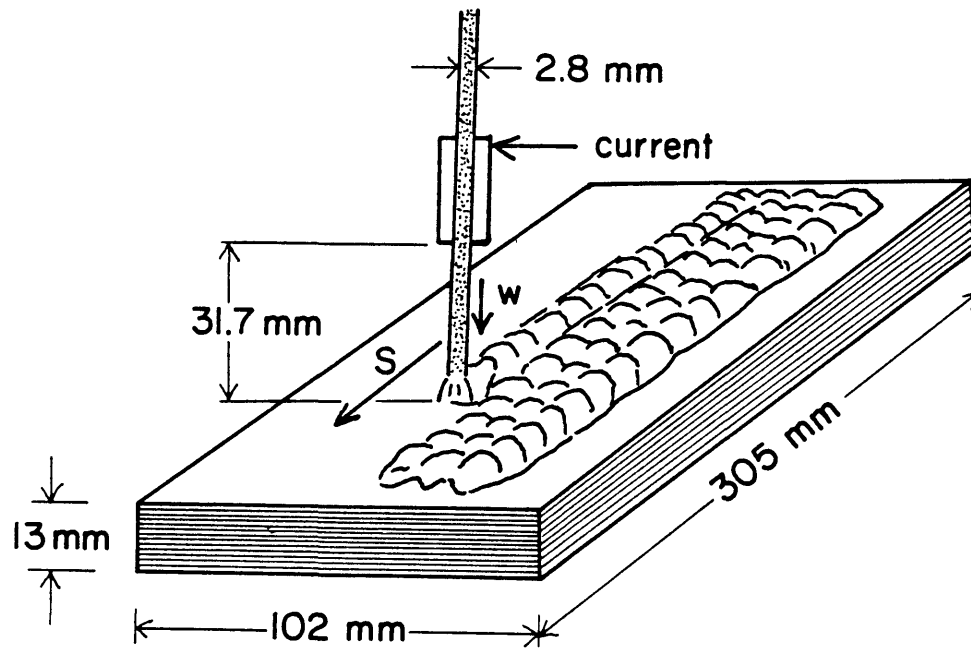
Figure 8.- Welding procedure for samples from matrix
1. 1020 steel plate was used, and welding
was done with the automatic flux-cored arc
welding process.

a: wear test I   d: wear test 3   g: macrostructure

b: wear test 2   e: microstructure

c: chemical analysis   f: wear test
                           (longitudinal)
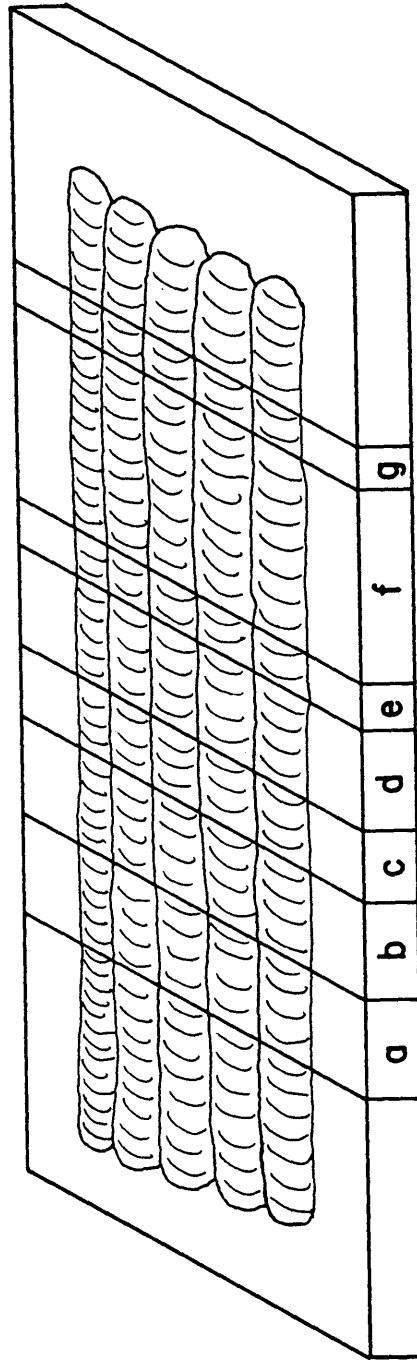
Figure 9.- Sectioning of samples from matrix 1 for subsequent analyses.

transversely only for abrasion testing and optical metallography.

2.5 SPECIMEN ANALYSES

2.5.1 Macrostructural Examination

Half-inch sections cut from all the test plates were ground and polished to 1 m alumina powder in the transverse direction, and macroetched using Vilella's reagent, whose composition is shown in Table 7:

Constituent	Quantity
HCl (aq)	5 cm3
Picric acid	1 g
CH3OH	100 cm3

Table 7.- Composition of Vilella's reagent, used for macroetching (33).

Dilution measurements were done by computing the ratio of cross-sectional area of the fusion zone below the surface of the base plate to the total fusion zone cross-sectional area:

$$\% \text{ Dilution} = \frac{B}{T} \times 100 \qquad (5)$$

where B = cross-sectional area of fusion zone below

            level of base plate

       T = total cross-sectional area of fusion zone

2.5.2 Chemical Analysis

Three-quarter-inch sections were cut and ground down to approximately the same depth range where abrasion testing was done (~3 mm from the top of the beads). Analyses were done using a Baird-Atomic Spectromet emission spectrometer, which gave data for 8 elements.

2.5.3 Optical Metallography

The sections cut for metallography were further sectioned into smaller pieces so that mounting and polishing would be easier. Polishing was done down to 0.05 μm alumina powder in the transverse direction. The polished sections were etched with the same reagent used for macroetching (see Table 7), after which representative photomicrographs were taken at a depth corresponding approximately to where abrasion tests were conducted. Measurement of volume fractions of the phases present was done using conventional

point-counting techniques (34). Other microstructural
parameters like average carbide radius and mean free path
between carbides were calculated from the following measured
quantities (35):

N_A = # of particles/unit area

N_L = # of particles/unit length of line

The equations used were:

Average particle radius $r = \dfrac{2}{\pi} \dfrac{N_L}{N_A}$ (6)

Volume fraction $f = \dfrac{8}{3\pi} \dfrac{N_L^2}{N_A}$ (7)

Mean free path $\lambda = \dfrac{1-f}{N_L}$ (8)

2.5.4 Abrasion Testing

For matrix 1, four pieces were cut from each test plate
for abrasion testing, as shown in Figure 9. For matrix 2,
only two specimens were tested from each plate, because
relatively small deposits were made. They were all ground
down to 600 grit to provide the smooth surface required for
abrasion testing. Only porosity-free surfaces were used,

and in cases where there was extensive porosity, some of the pieces were rejected. Testing was done according to ASTM Standard G-65-80, "Conducting Dry Sand/Rubber Wheel Abrasion Tests" (18). Figure 10 is a schematic of the testing fixture. The standard procedures were followed with a force of 130 N on each sample and 6000 revolutions per test. Figure 11 shows the direction of rotation of the rubber wheel with respect to both the longitudinal and transverse samples.

2.5.5 Scanning Electron Microscopy

The surface of the wear samples of all alloys was examined after abrasion testing. An AMR 1200 Scanning Electron Microscope was used.
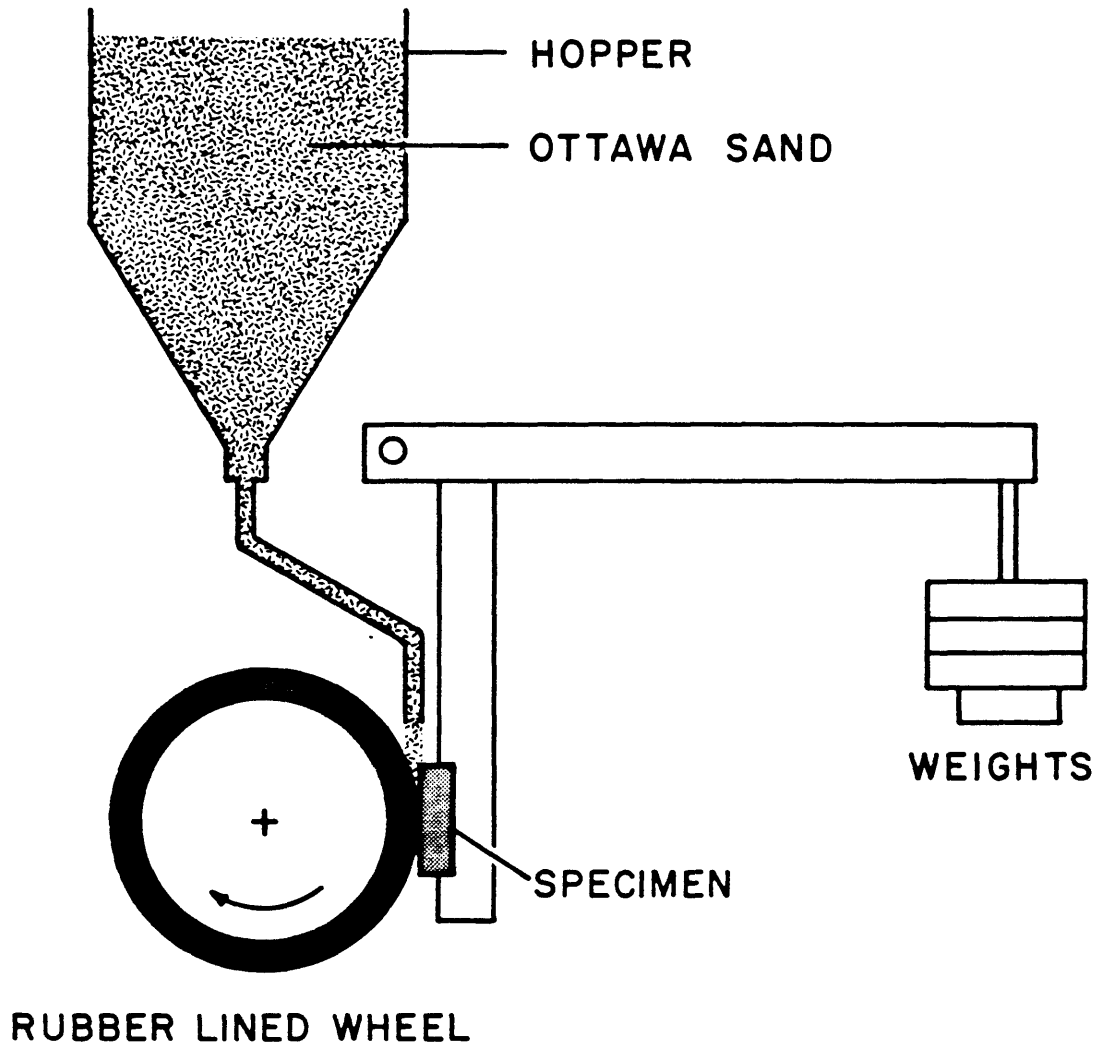
Figure 10.- Schematic of the Dry Sand/Rubber Wheel
Abrasion Test (ASTM G-65-80).

Transverse
Test
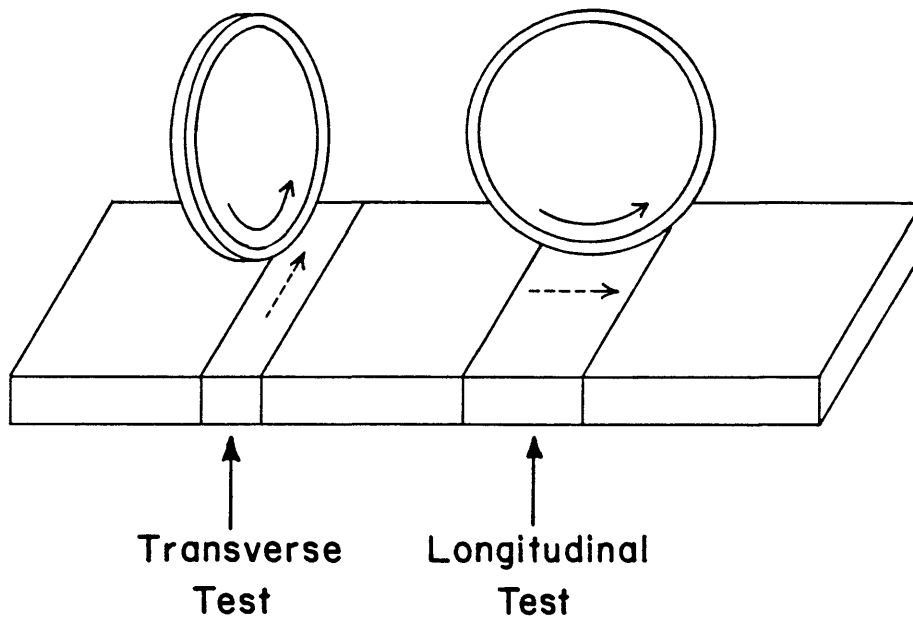
Longitudinal
Test

Figure 11.- Direction of rotation of rubber wheel
            with respect to both longitudinal and
            transverse samples in the Dry Sand/
            Rubber Wheel Abrasion Test.

3 RESULTS AND DISCUSSION

The results obtained from the process-parameter study on a single TiC-type hardfacing alloy (matrix 1) will first be presented and discussed. As explained in detail in the previous chapter, a commercial alloy was deposited at different values of current, voltage and travel speed in a systematic way, so that variations in macrostructure, microstructure, chemistry and abrasion resistance of the deposits could be examined. Matrix 2 and its results will then be discussed. It involved varying the alloy chemistry to investigate the effects of changing the carbide volume fraction and the matrix composition.

3.1 EFFECTS OF PROCESS PARAMETERS ON THE CHARACTERISTICS OF A COMMERCIAL TiC-BASED HARDFACING ALLOY (MATRIX 1)

The experimental results of this part of the investigation can be broken down into macrostructural variations, chemical variations, microstructural variations and abrasion resistance. The commercial alloy used will be referred to as alloy A.

3.1.1 Macrostructural Variations

The morphology of the hardfacing overlays was observed
to change systematically with changes in welding process
parameters. Figure 12 shows top-view photographs of
selected test samples illustrating the bead-shape
differences. The most obvious influence was that from heat
input: at a low heat input (1 MJ/m), the individual beads
were narrow, bulky and convex in shape; while at 2 MJ/m they
were relatively smooth and covered a larger area of the base
plate.

Penetration and dilution changes can be observed in
Figure 13, which shows the cross-sections of the deposits
from Figure 12. The increase of dilution with increasing
heat input is shown quantitatively in Figure 14. Even
though heat input is probably the most important factor in
determining the extent of melting of the base plate and thus
the dilution, the spread of dilutions at a given heat input
in Figure 14 indicates that other factors must be involved.
Figure 15 shows a map of the metal transfer modes which were
observed as a function of location in V-I process space.
These modes are shown schematically in Figure 16. Note that
all of the low heat-input deposits were produced under
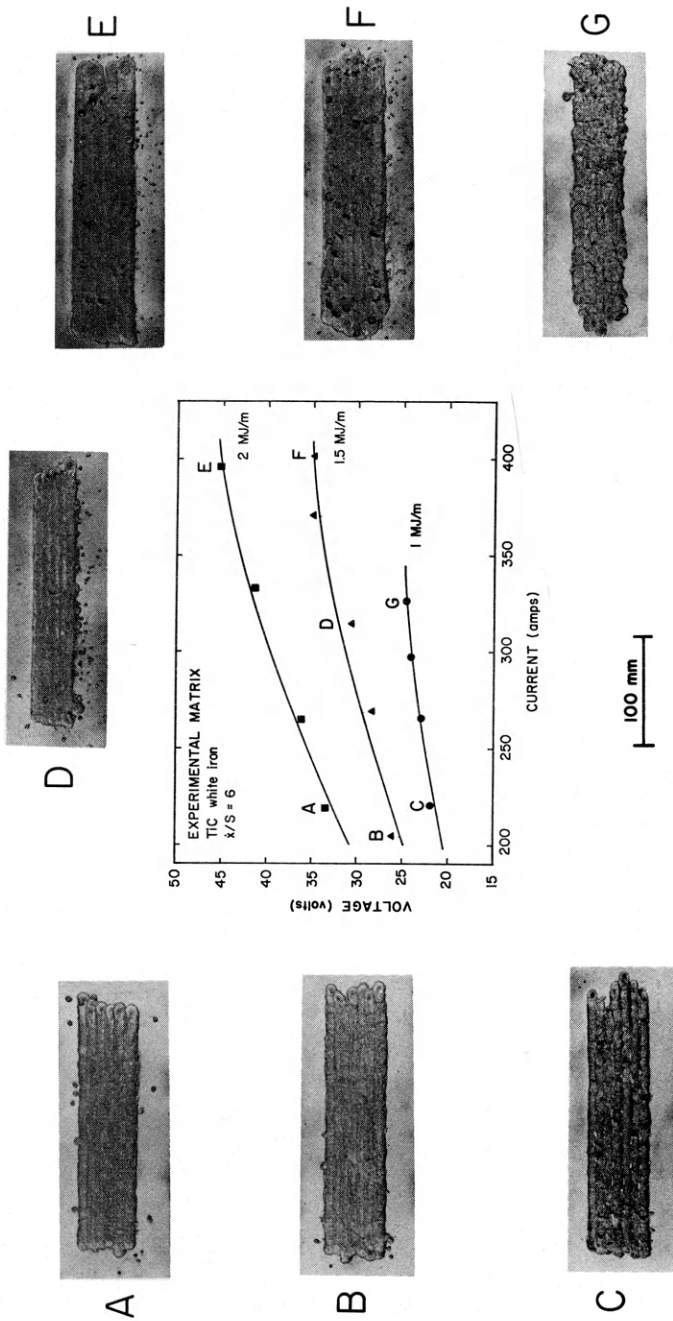
Figure 12.- Top-view photographs of hardfacing deposits from alloy A welded at the indicated values of current and voltage.
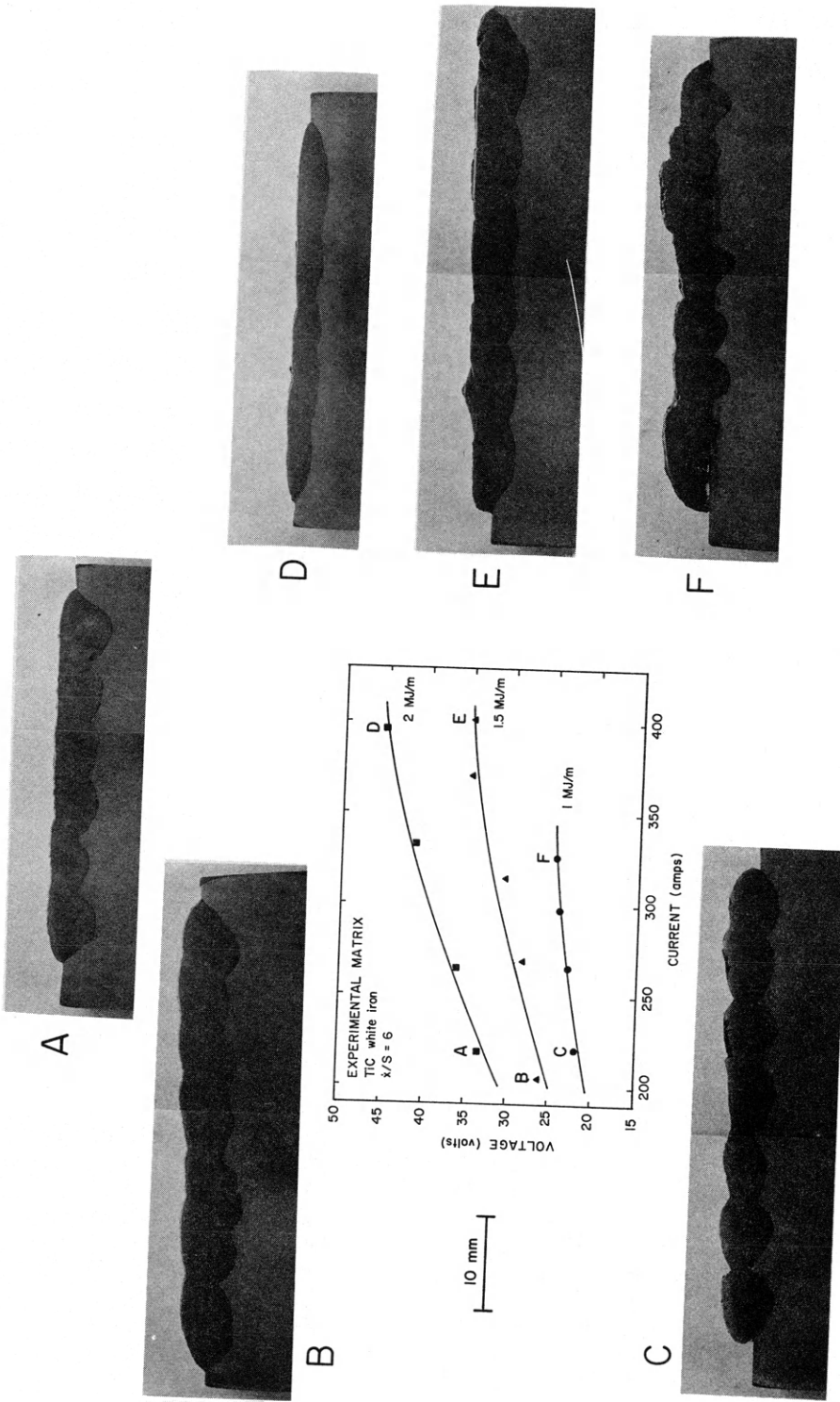
Figure 13.- Transverse cross-sections of the deposits shown in Figure 12.
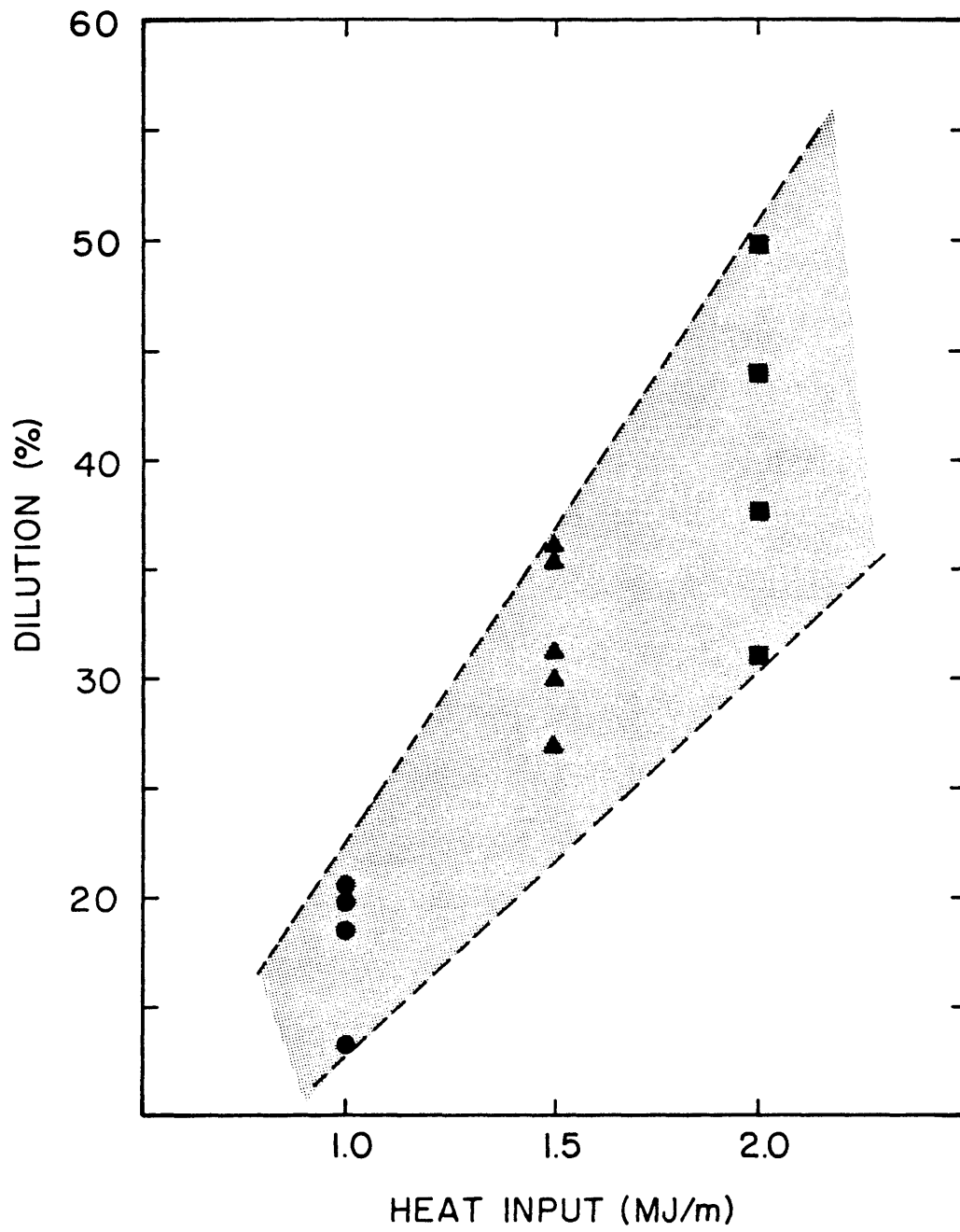
Figure 14.- Influence of heat input on dilution.
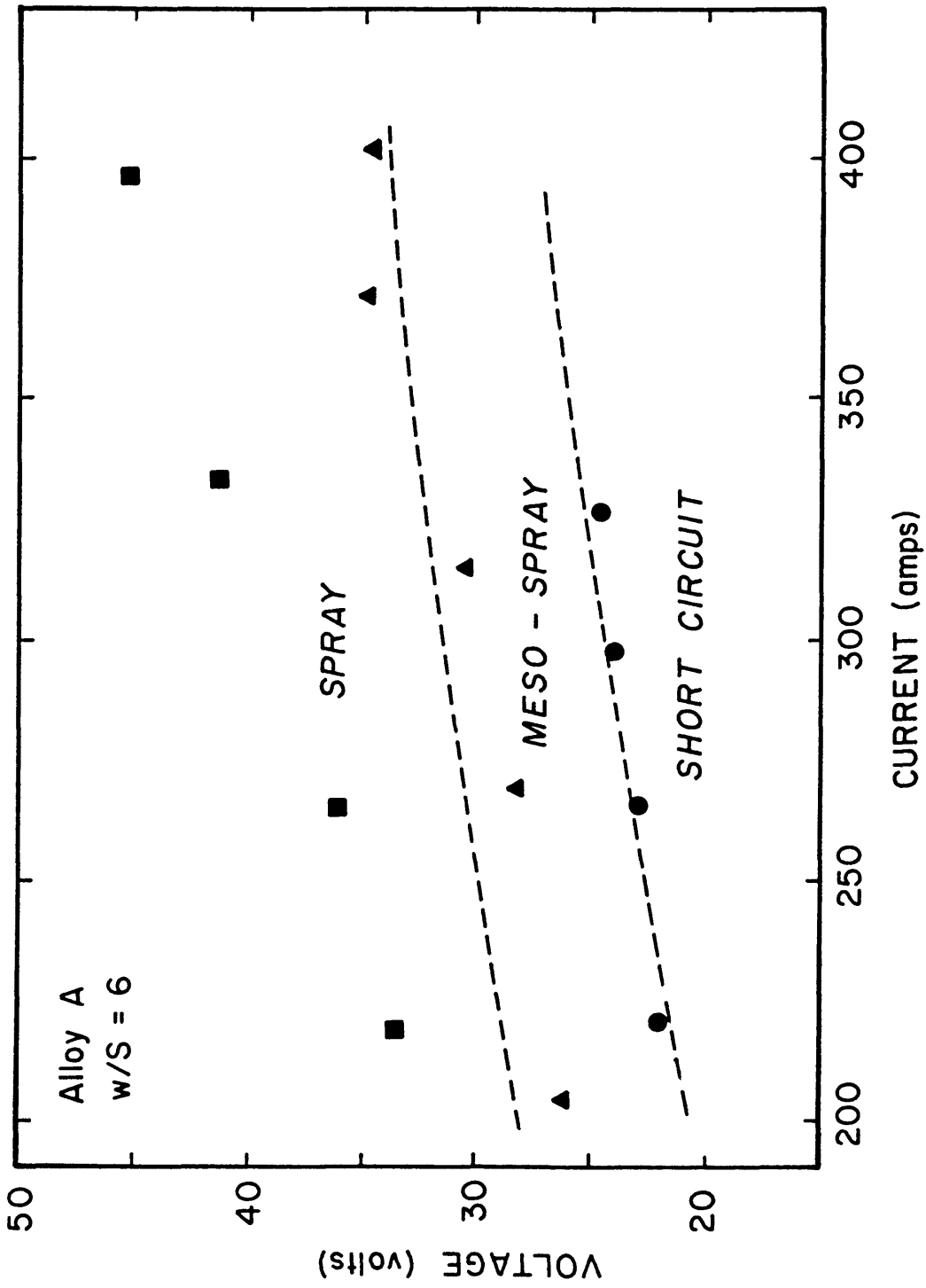
Figure 15.- Map of the observed transfer modes in V - I process space.
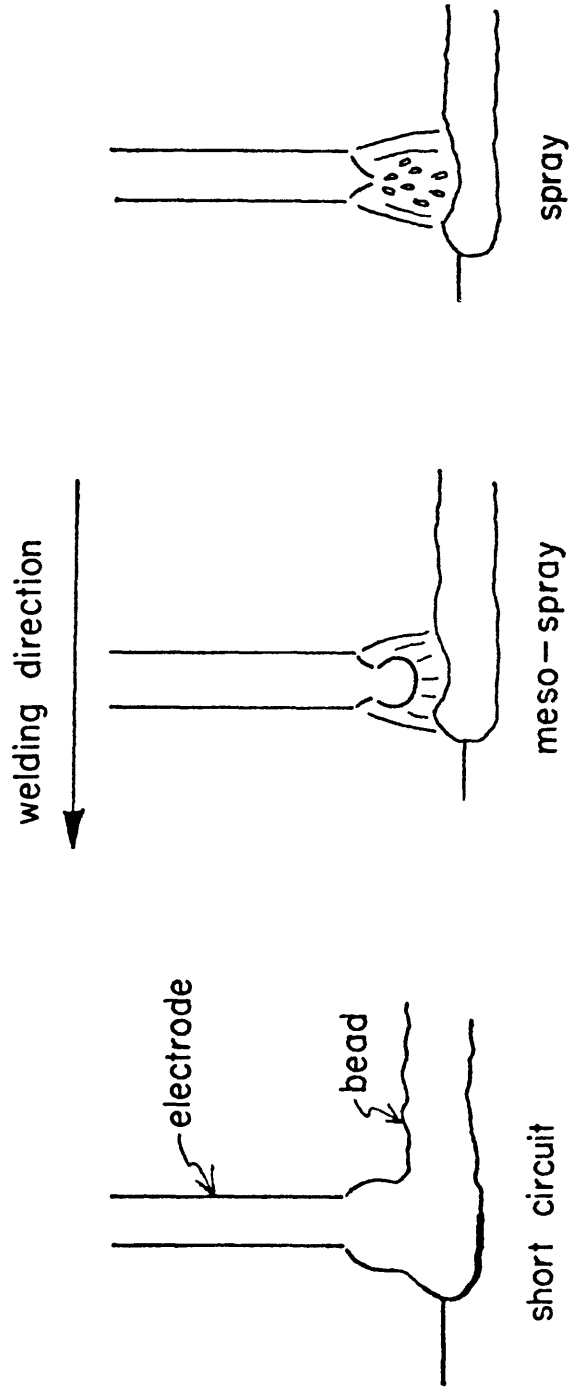
Figure 16.- Schematic of the three metal-transfer modes observed during the welding of alloy A at different process parameters.

conditions close to the short-circuit transfer mode, in
which there is only intermittent arcing between the
electrode and the molten pool. Increasing the heat input to
1.5 MJ/m meant increasing the voltage to the point where
there was continuous arcing and transfer was in the
meso-spray mode. At the larger voltages the metal was
observed to be transferred in tiny droplets blown away by
the arc, which approaches a spray type of transfer. Thus it
was found that if the deposition ratio is kept constant, it
is the voltage that controls the transfer mode and thus the
bead morphology.

For a given transfer mode, dilution decreased with
increasing currents, as illustrated in Figure 17. This
effect may be visualized as follows. Consider two welds
produced using the same transfer mode, one at low current
and one at high current (plates C and F in Figure 13).
Specimen C was deposited at low power input (VI) and at a
relatively low travel speed (S); even though there is a
relatively low electrode melting rate, the slow weld travel
speed allows sufficient time for the heat generated in the
arc plasma and cathode spot to be conducted into the base
plate. Specimen F was produced using a higher power input,
but the weld travel speed was increased to insure the same
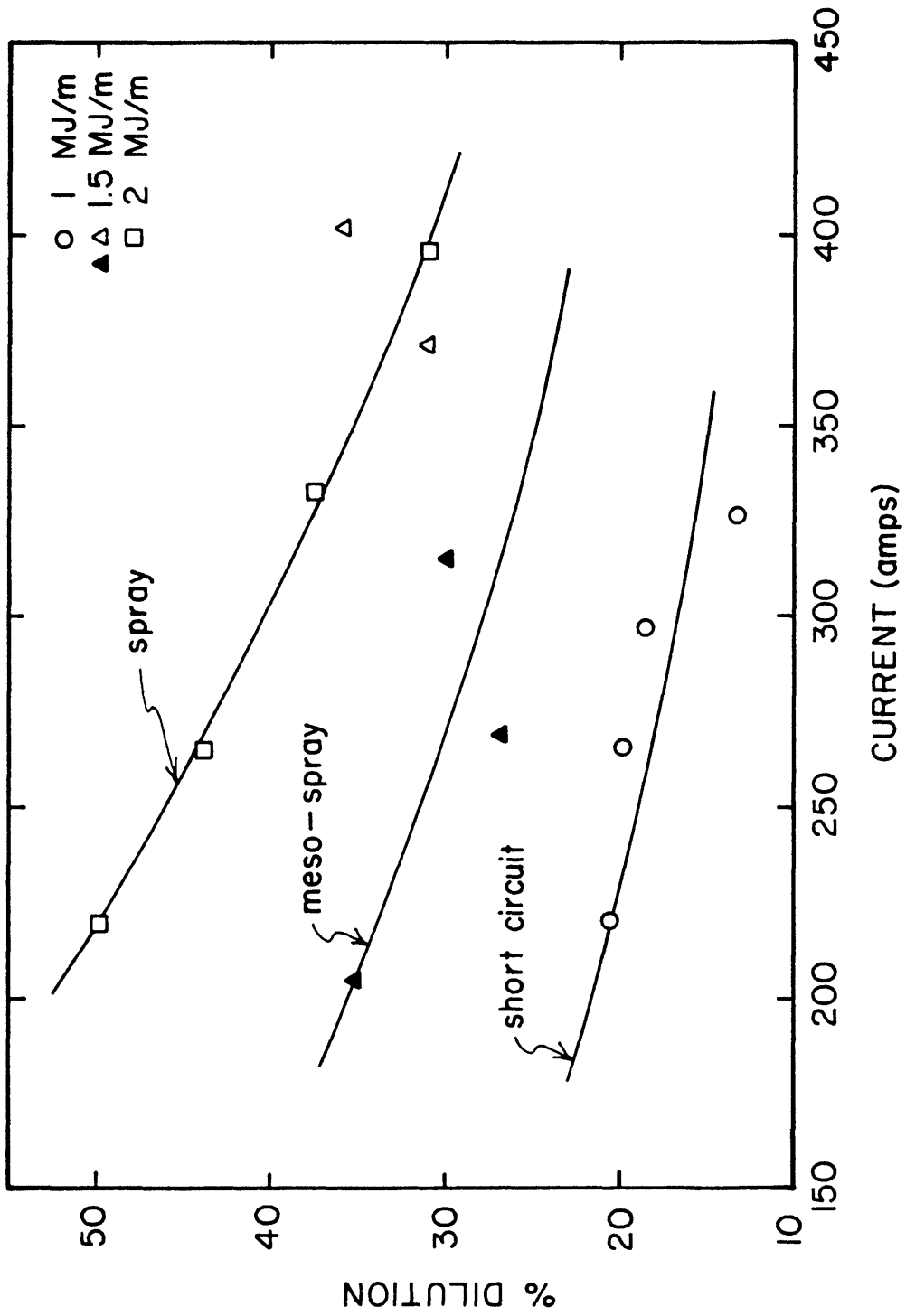
Figure 17.- Effect of current on dilution at a given transfer mode.

nominal value of heat input (H) as given by equation 4. In

this case the torch is moving fast enough that the heat does

not have time to melt as much of the plate before cooling

begins. Thus, the thermal cycle at a given point on the

plate is faster for case F than for case C, yielding less

weld penetration. In addition, the high radiation heat

losses provided by the large arc gaps at high voltages tend

to reduce penetration even further.

Figure 12 shows porosity to be a problem in the region

where current and voltage are high. Here the metal transfer

approaches the spray mode, in which the metal goes through a

relatively large arc gap in the form of tiny liquid

droplets. Because of their large surface-area/volume ratio,

the droplets are able to pick up a significant amount of gas

from the arc plasma (especially O_2). This gas content is

then liberated during solidification causing porosity.

Assuming no metal losses during welding, a constant

deposition ratio would mean the same average cross-sectional

area per bead, measured above the level of the base plate.

Table 8 shows that there were variations in this area, which

reflects changes in the efficiency of metal transfer. As

shown in Figure 18, more material was lost (from spatter and

Table 8

Measured Cross-sectional Area per Bead Above the Top Surface of the Base Plate for all Hardfacing Deposits From Alloy A

Sample	Heat Input (MJ/m)	Current (amps)	Voltage (volts)	Cross-sectional Area Above Base Plate/Bead (cm^2)
1	1	221	22.0	0.258
2	1	266	23.0	0.284
3	1	298	24.1	0.268
4	1	327	24.6	0.287
5	1.5	205	26.3	0.229
6	1.5	269	28.4	0.259
7	1.5	315	30.7	0.250
8	1.5	371	34.9	0.273
9	1.5	402	34.9	0.251
10	2	219	33.5	0.221
11	2	265	36.2	0.220
12	2	333	41.4	0.221
13	2	396	45.2	0.254
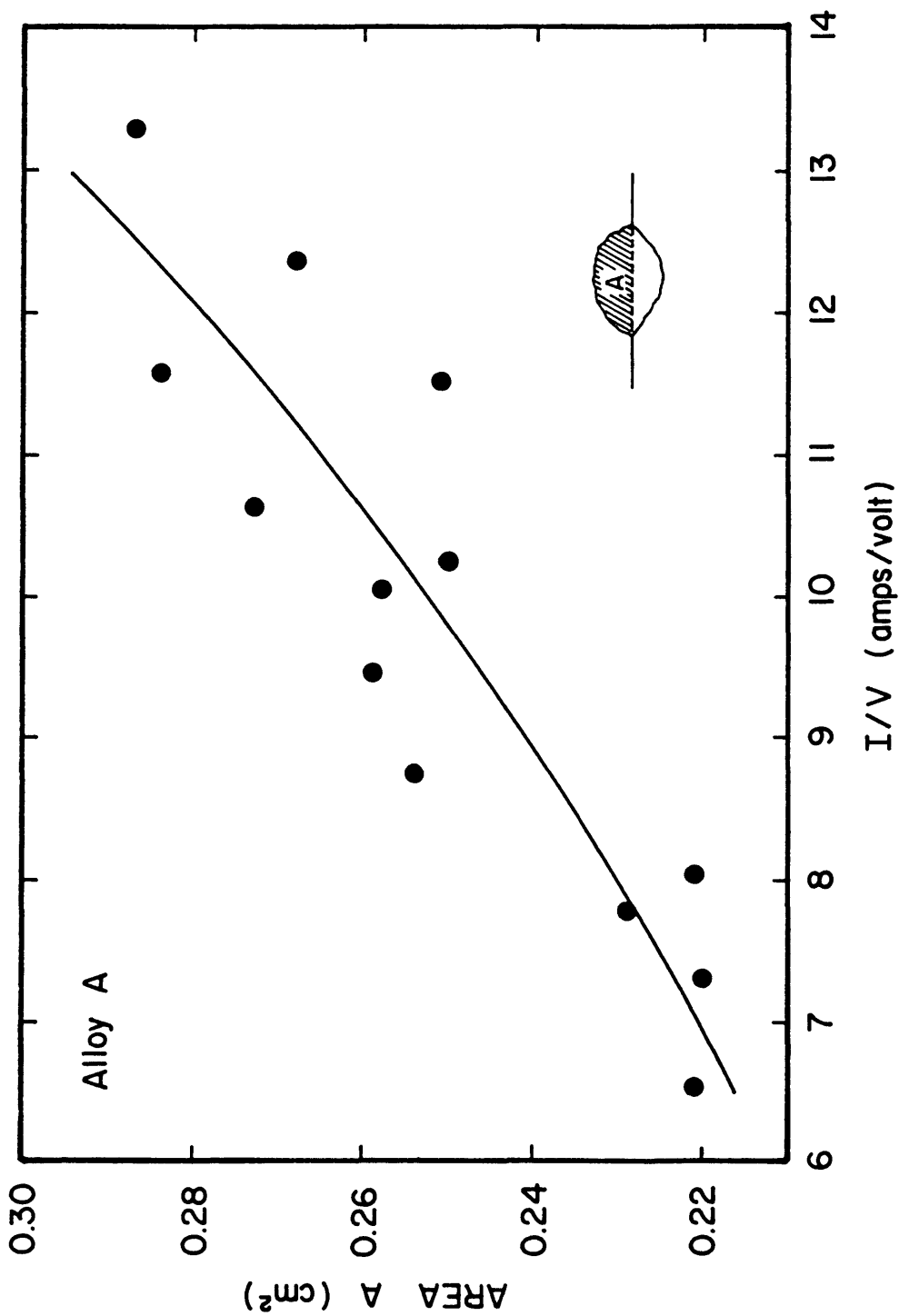
Figure 18.- Variation of the average cross-sectional area per bead, measured above the level of the base plate, as a function of the I/V ratio.

arc volatilization) as the I/V ratio decreased. Indeed, it was observed that the arc gap increased as the I/V ratio decreased.

3.1.2 Chemistry Variations

The results of chemical analyses appear in Table 9. These show that the most significant alloying elements are chromium and carbon. Figure 19 shows that the chromium content decreased with increasing dilution. This would be expected, since the steel base-plate contained almost no chromium. Figure 20 shows a similar behavior for the total carbon content. While other minor alloying elements also show similar trends, the carbon and chromium variations will be used to explain microstructural changes, as they represent the major constituents.

3.1.3 Microstructural Variations

The general microstructure of the deposits consists of a Cr-white iron matrix containing small particles of titanium carbide (TiC) more or less evenly distributed throughout the microstructure. Figure 21 shows a typical microstructure of one of the weld overlays from this study.

Table 9

Chemical Compositions of TiC-type Hardfacing Deposits From Matrix 1

Sample	Heat Input (MJ/m)	Current (amps)	Voltage (volts)	C	Si	Mn	Mo	Cr	Ni	Cu	P
1	1	221	22.0	2.83	0.13	1.23	0.06	4.1	0.05	0.07	0.005
2	1	266	23.0	4.50	0.11	1.49	0.06	6.5	0.04	0.03	0.005
3	1	298	24.1	3.97	0.11	1.52	0.06	6.2	0.04	0.03	0.005
4	1	327	24.6	4.60	0.10	1.65	0.06	7.2	0.04	0.02	0.005
5	1.5	205	26.3	2.72	0.12	1.38	0.05	4.2	0.07	0.12	0.005
6	1.5	269	28.4	2.93	0.12	1.43	0.06	4.9	0.06	0.07	0.005
7	1.5	315	30.7	3.05	0.12	1.43	0.06	4.6	0.06	0.08	0.005
8	1.5	371	34.9	3.40	0.13	1.31	0.06	5.0	0.06	0.07	0.005
9	1.5	402	34.9	2.83	0.13	1.23	0.06	4.1	0.05	0.07	0.005
10	2	219	33.5	1.74	0.14	1.17	0.05	3.1	0.09	0.17	0.005
11	2	265	36.2	1.95	0.13	1.16	0.05	3.3	0.08	0.16	0.005
12	2	333	41.4	2.40	0.13	1.08	0.06	3.4	0.07	0.13	0.005
13	2	396	45.2	3.14	0.13	1.27	0.06	4.7	0.06	0.07	0.005

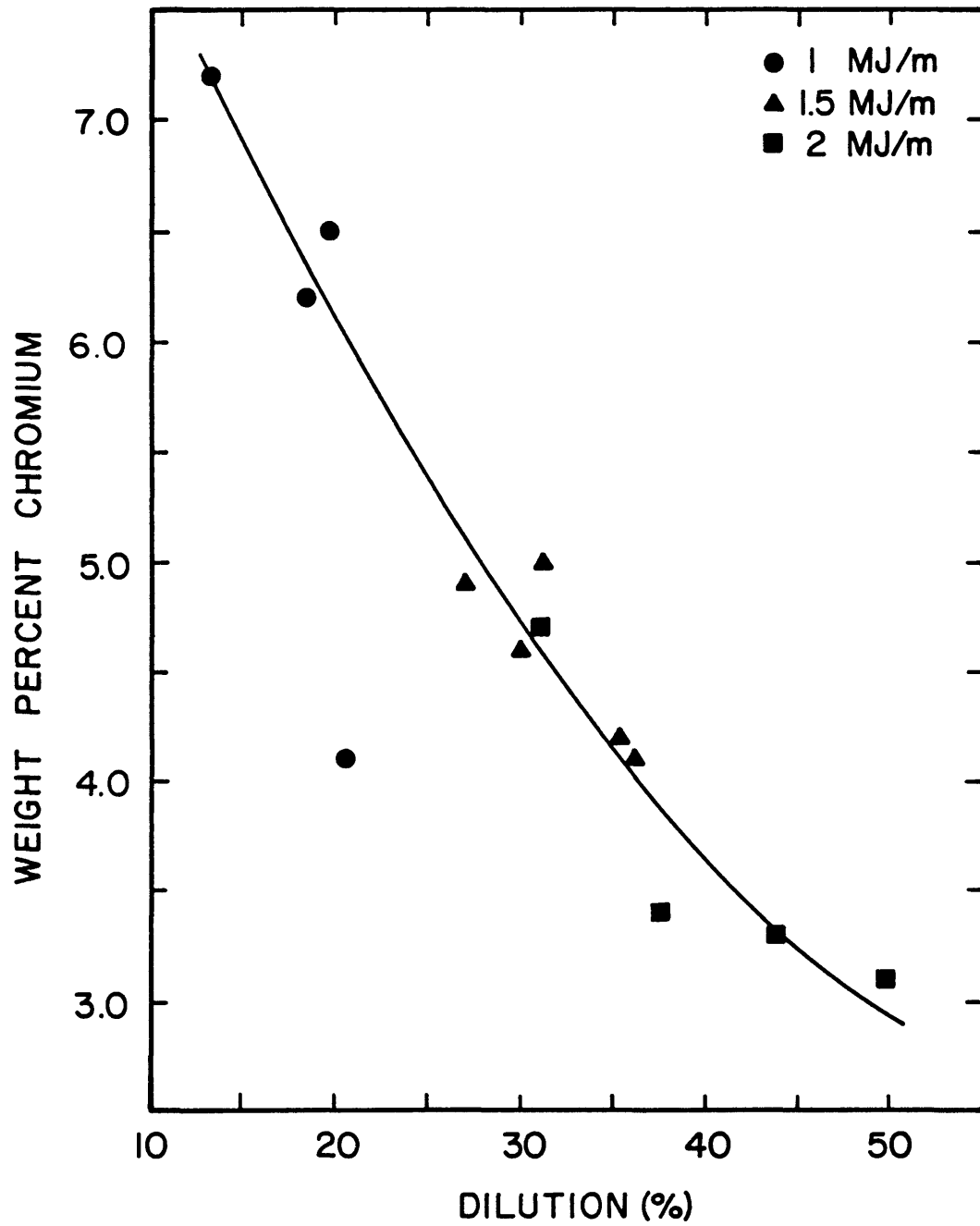Figure 19.- Variation of chromium content with dilution
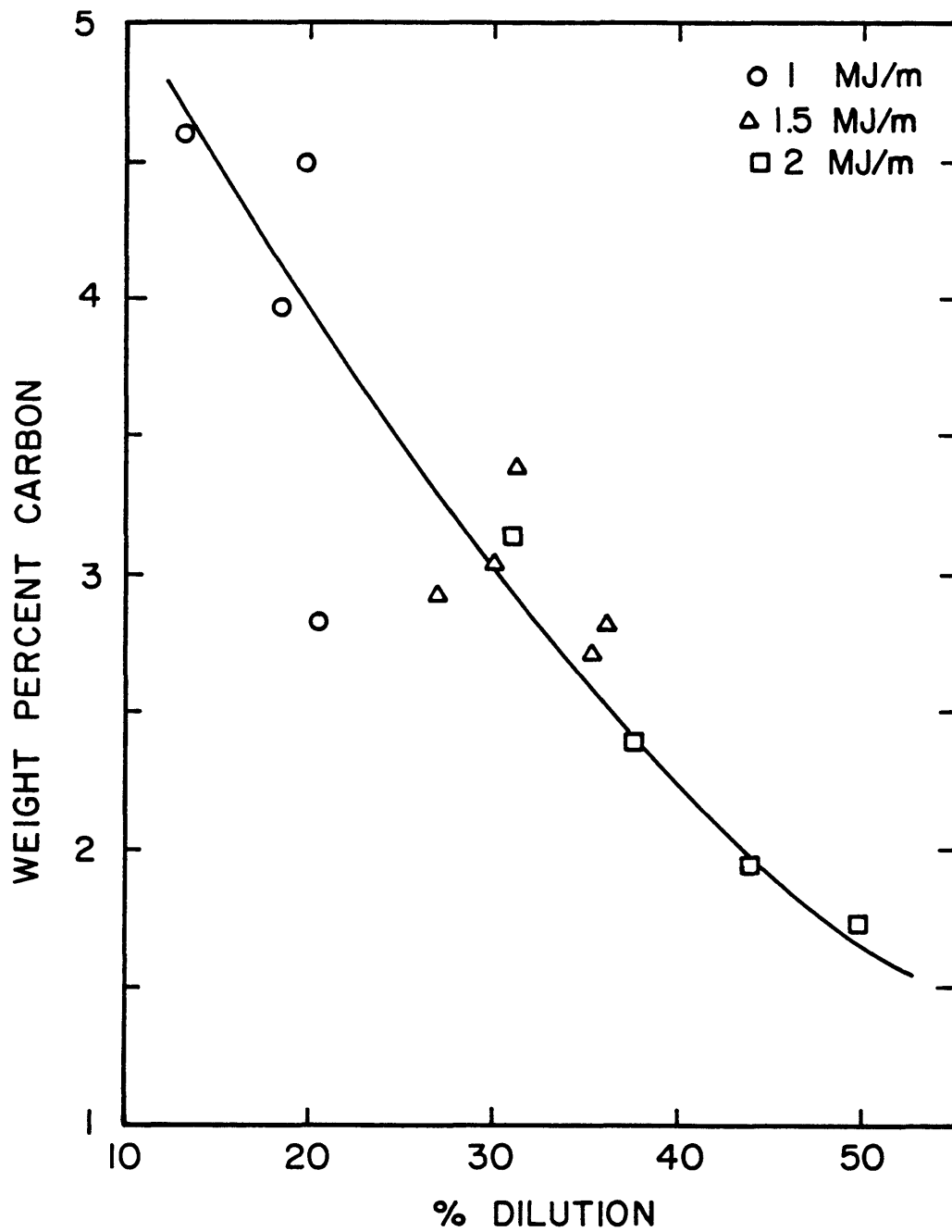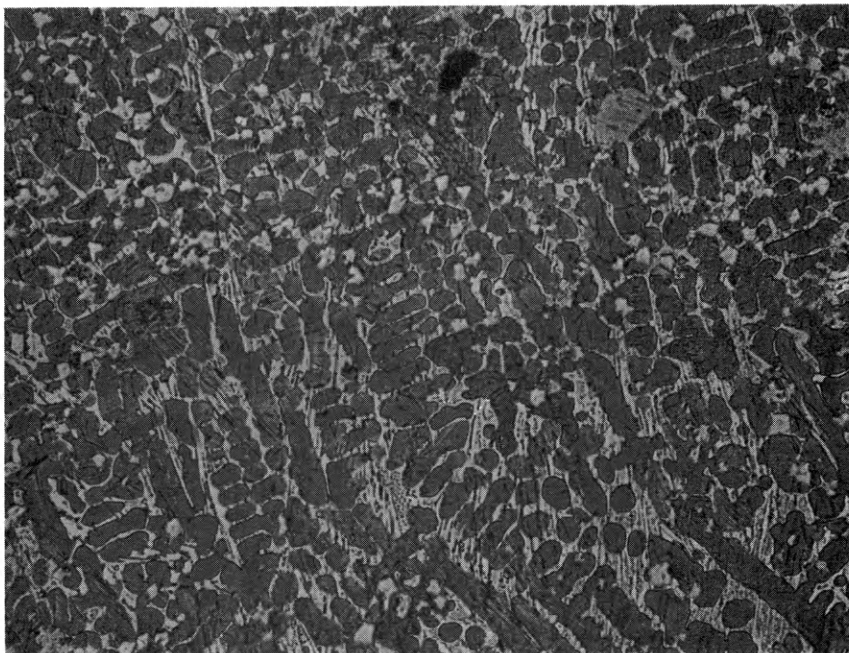for alloy A.

Figure 20.- Variation of carbon content with dilution
          for alloy A.

(b) Etched in Villela's Reagent

50 μm

(a) Unetched

Figure 21.- Typical microstructure of alloy A.

The unetched micrograph (21-a) reveals the titanium carbides only. Note that they are irregular in both size and shape mainly because they were not formed during solidification but were transferred in the solid state across the welding arc. In Figure 21-b, the polished surface was etched to reveal the matrix solidification structure. The dark phase corresponds to austenite (γ) dendrites which solidified first in the weld pool. The carbon content of about 3% and chromium content of about 7.5% place the alloy in the γ + liquid region of the Fe-C-Cr ternary liquidus diagram. With cooling below the liquidus, the austenite dendrites reject chromium and carbon to the remaining liquid until a pseudo-eutectic reaction L $\rightarrow$ (Fe,Cr)$_3$C + γ occurs (21). This reaction occurs over a relatively narrow temperature range until solidification is complete. The interdendritic eutectic structure comprised of (Fe,Cr)$_3$C + γ, known as ledeburite, shows up in Figure 21-b as a light phase (cementite) with dark spots (γ). With further cooling, the solubility of carbon and chromium in austenite decreases, and a temperature is finally reached where austenite is no longer stable under equilibrium conditions. The cooling rates in a weldment are too fast for any appreciable solid-state diffusion to occur; therefore, the austenite dendrites either remain as retained meta-stable austenite or

undergo a shear transformation to martensite, depending
mainly on alloy content.

Figure 22 illustrates the influence of welding process
variables on the microstructure of the test deposits. As
expected, a systematic variation was observed with the
amount of dilution. The volume fractions of $(Fe,Cr)_3C$
(cementite) and TiC are plotted in Figure 23 against percent
dilution. It was observed that the volume fraction of
cementite changed dramatically with dilution, but that of
TiC stayed relatively constant. The cementite variation was
caused by relatively large decreases in the chromium and
carbon contents with increasing dilutions, as shown in
Figures 19 and 20. Thus at the higher dilutions (low
current and high voltage), the carbon and chromium
concetrations are so low in the weld pool that they are
completely soluble in the austenite phase. The net effect
is a matrix with no ledeburite (micrograph A in Figure 22).
On the other hand, micrograph F in Figure 22 shows the
highest volume fraction of ledeburite where dilution was the
lowest (highest I/V ratio). The slight decrease in the TiC
volume fraction was caused by the slight increase in the
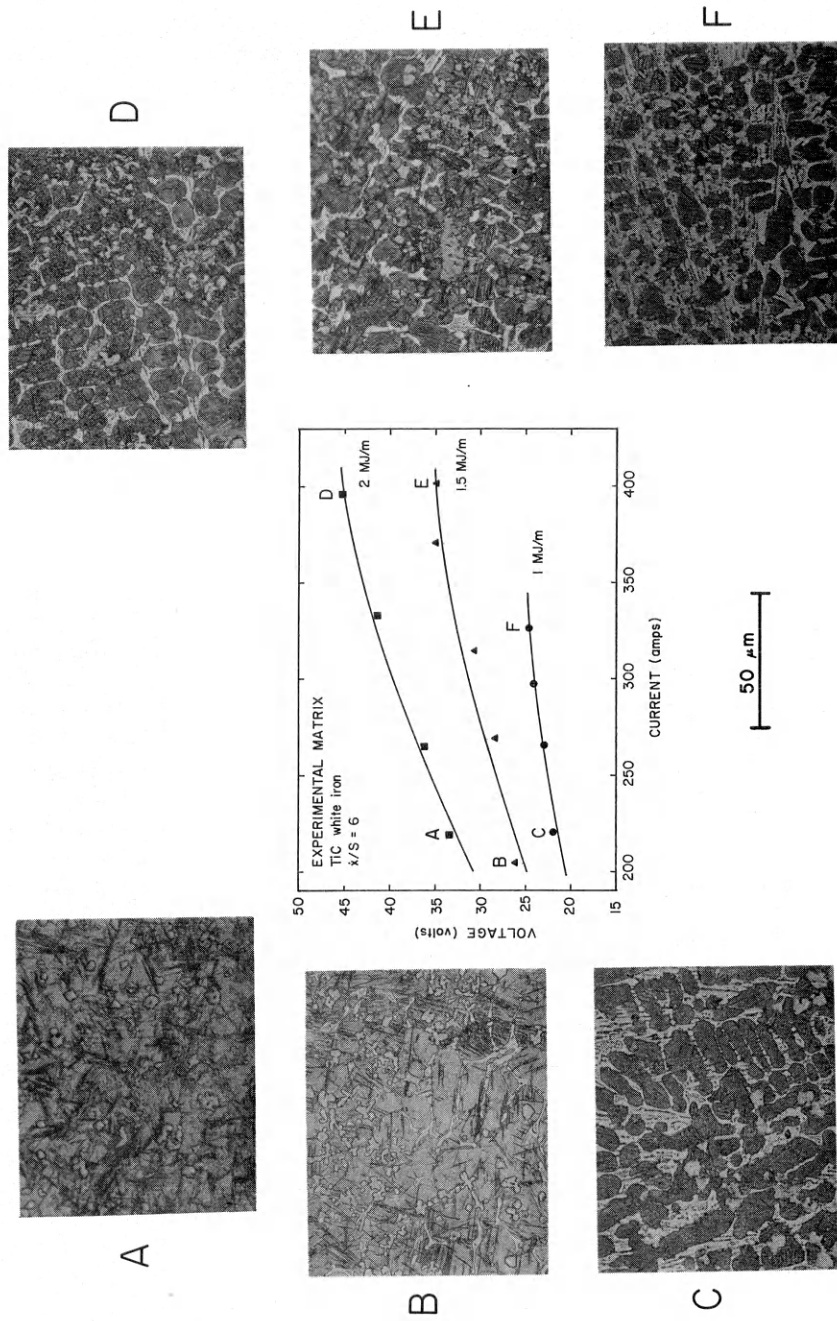fusion-zone size with increasing heat input.

Figure 22.- Influence of welding process variables on the microstructure of alloy A.
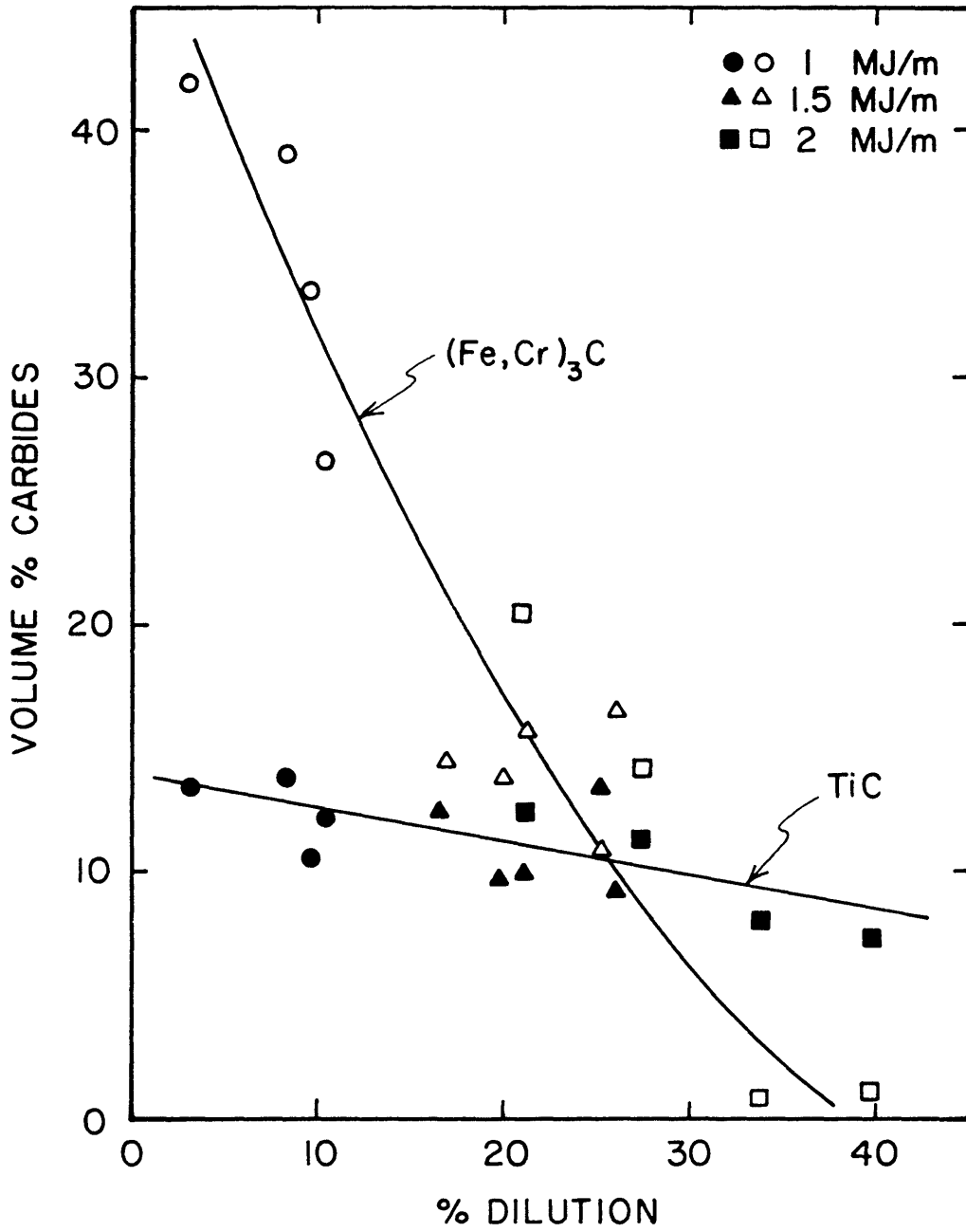
Figure 23.- Effect of dilution on the volume fractions of titanium carbide (TiC) and cementite ((Fe,Cr)$_3$C) in alloy A.

Heat input did not have any obvious effect on the
coarseness of the microstructures, as can be seen in the
micrographs of Figure 22. This may be because the range of
heat inputs used was not big enough to cause a large
difference.

A final microstructural observation was that the nature
of the austenite transformation product was influenced by
the process parameters. The expected change in the
martensite-start (M_s) temperature is a monotonically
increasing function. Each of the alloy constituents serves
to "stabilize" the austenite by obstructing the shear
mechanism of the martensitic transformation. Consequently,
the martensitic reaction is more likely to occur as the M_s
temperature increases or as dilution increases. This
increase in martensite content with dilution is shown in
Figure 24. The magnetic susceptibility of the hardfacing
deposit was measured using a Forrester Ferrite Content Meter
and plotted as a function of dilution. If the dilution
increased beyond about 38%, however, the bainite reaction
transformed the austenite before martensite could be formed.
The micrographs in Figure 22 illustrate the effect of
dilution on the martensite content of the hardfacing
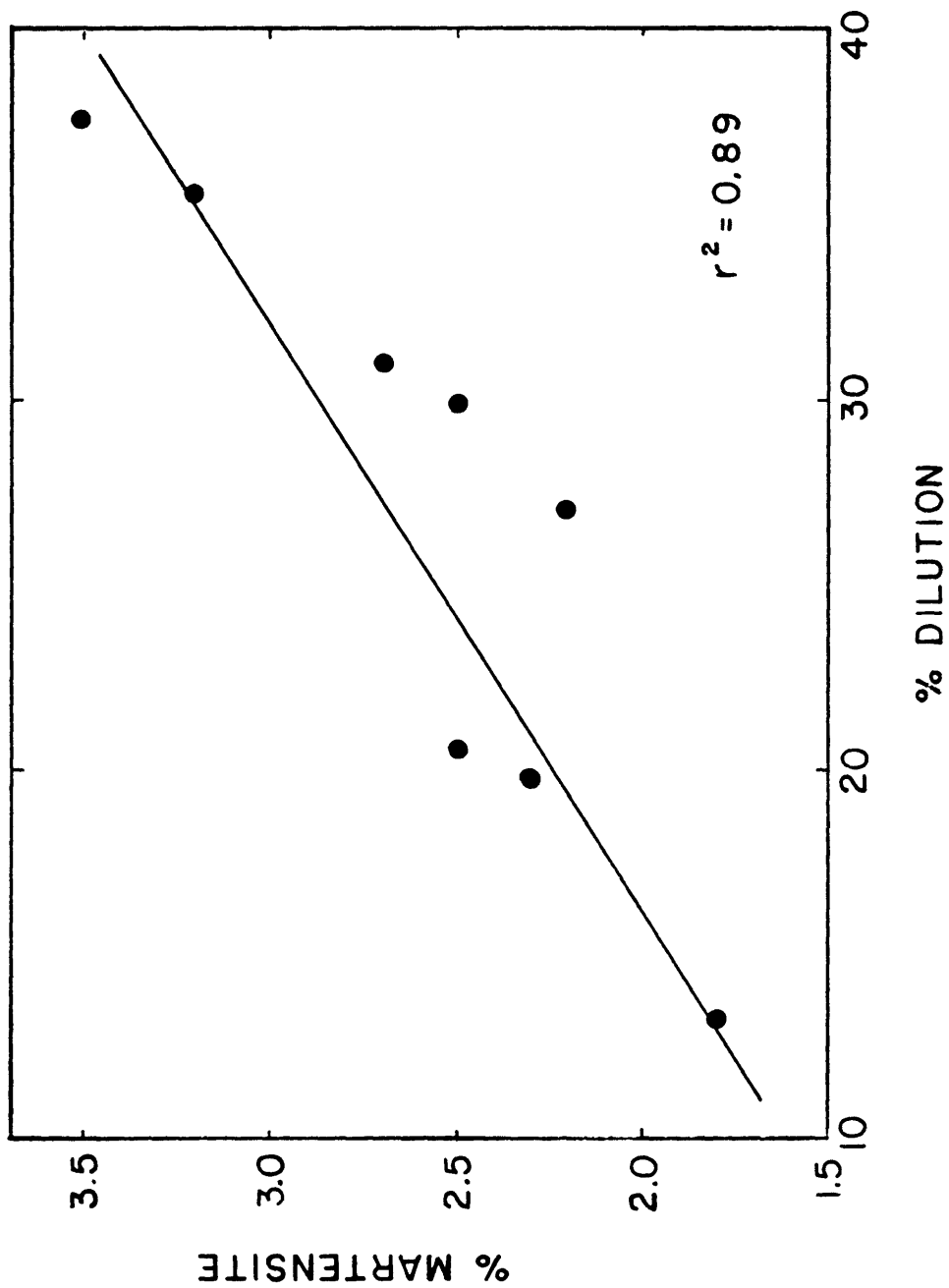deposits. In the low dilution deposits, the carbon and

Figure 24.- Effect of dilution on the amount of martensite in the microstructure of hardfacing alloy A.

chromium contents of the austenite phase were high, the M_S was low, and high amounts of retained austenite (micrographs F,C) were obtained. As dilution increased and carbon and chromium contents decreased, the M_S temperature was raised and the volume fraction of martensite increased.

3.1.4 Abrasion Test Results

Weight losses from the ASTM Dry Sand/Rubber Wheel abrasion test are shown in Figure 25 as a function of dilution. Weight losses were reported instead of volume losses because of the difficulty in calculating the density of the hardfacing deposits. For comparison purposes, the plot also includes data from a similar investigation of a commercial high-Cr white iron hardfacing alloy (31). The TiC-type alloy exhibited a very good abrasion resistance throughout the whole range of process parameters used for deposition. Even though the matrix microstructure was strongly influenced by dilution, the abrasion resistance remained essentially constant. This fact suggests that the abrasion resistance was controlled by the titanium carbides in the microstructure and that the changes in the matrix microstructure had little or no effect in the performance of the alloy. Figure 23 indeed shows that even the highest
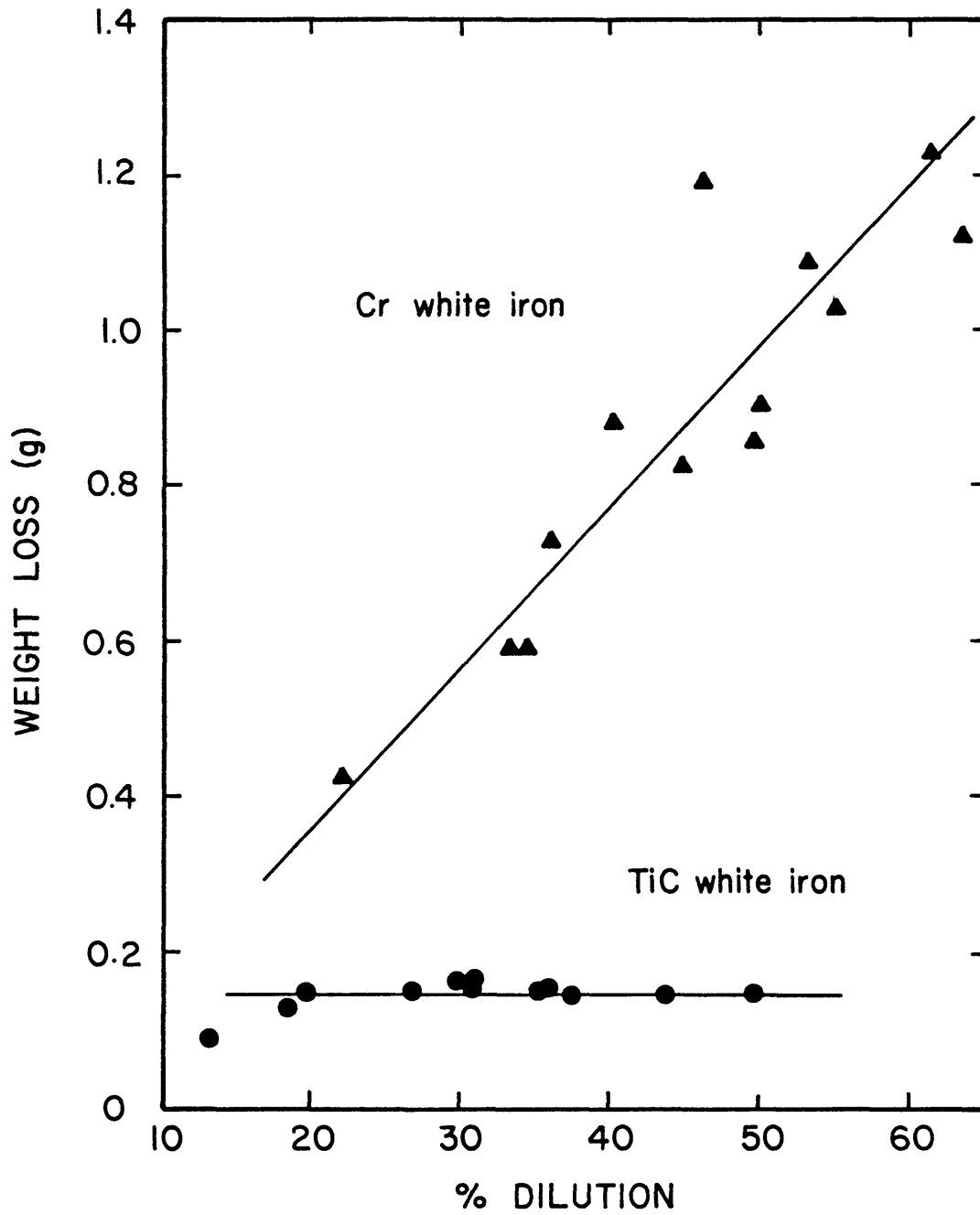
Figure 25.- Weight loss data for alloy A compared to a
Cr white iron (31) as functions of dilution.
Weight losses are from the standard ASTM
Dry Sand/Rubber Wheel Abrasion Test.

dilutions observed were not sufficient to significantly alter the volume fraction of the TiC particles in the microstructure.

3.2 EFFECTS OF CHANGING THE MICROSTRUCTURE (MATRIX 2)

It seemed from the results of matrix 1 that the performance of alloy A under low-stress abrasion conditions was unaffected by the nature of the matrix material holding the carbides, and that, for a given carbide size, it was the volume fraction of the carbides that controlled abrasion resistance. To further investigate these observed effects, and to determine a mechanistic explanation of what goes on during the abrasion process, alloys 1 through 4 were tested using the ASTM Dry Sand/Rubber Wheel Abrasion Test.

3.2.1 Metallography

The microstructures of alloys 1, 2, 3 and 4 are shown in Figures 26, 27, 28 and 29 respectively, in both the unetched and etched conditions. The unetched micrographs show the carbide structure while etching reveals the matrix characteristics. As predicted, alloy 2 showed a larger volume fraction of carbides than alloy 1, and exhibited a
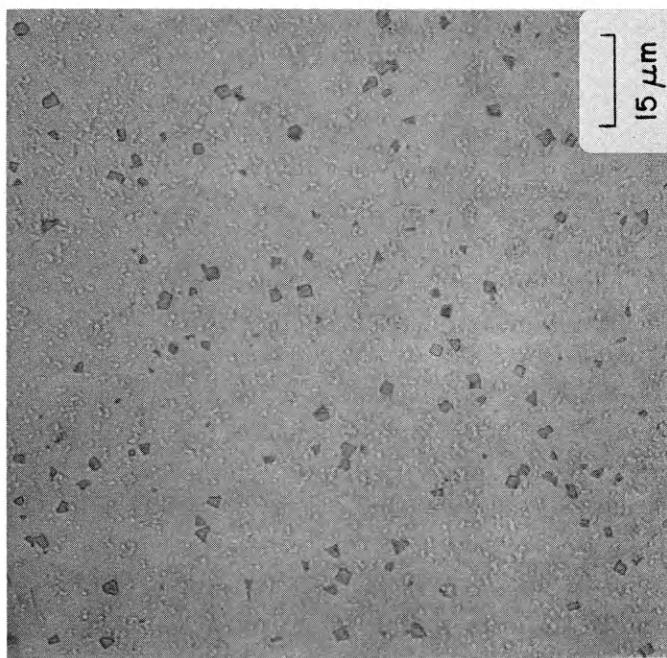
(b) Etched in Villela's Reagent

(a) Unetched
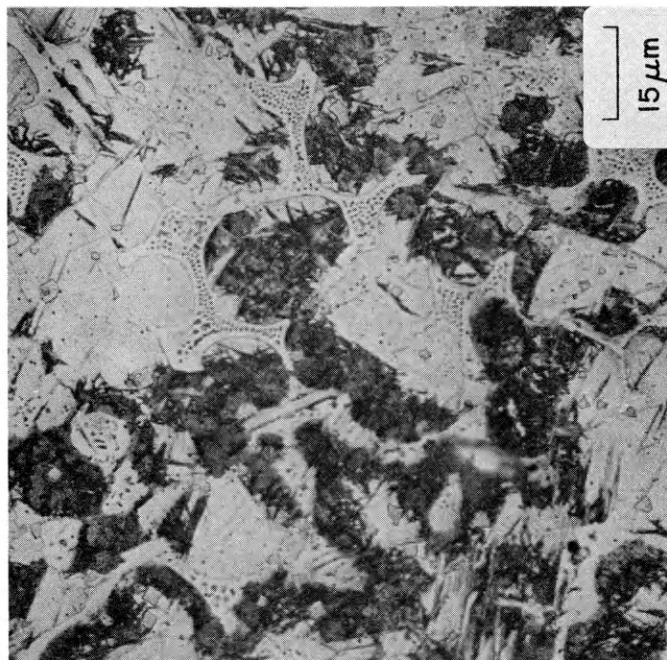
Figure 26.- Microstructures of alloy 1. Figure (a) shows the dispersed titanium carbides and Figure (b) shows the matrix structure, consisting of austenite (gray), martensite (dark), and interdendritic ledeburite (light with dark spots).
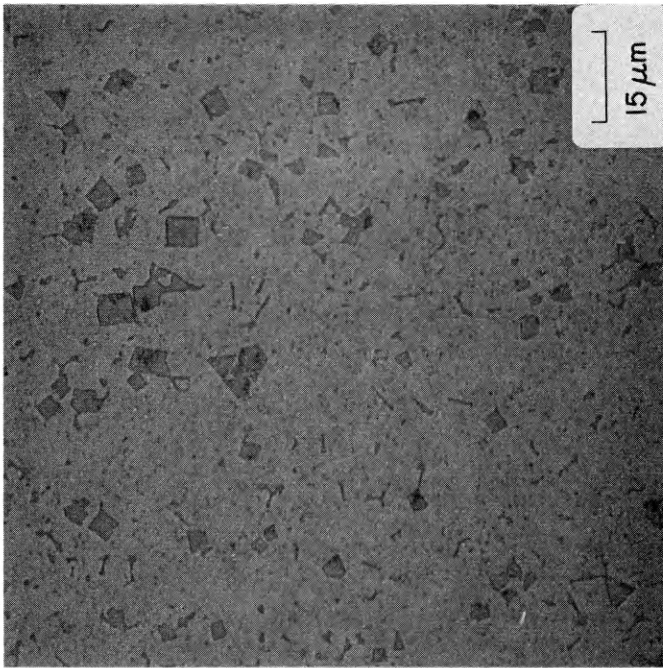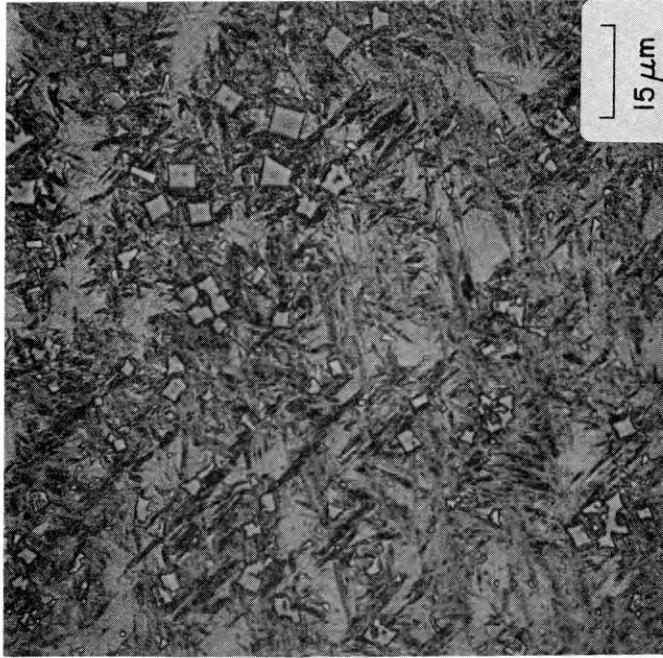
(b) Etched in Villela's Reagent

(a) Unetched

Figure 27.- Microstructures of alloy 2. The matrix structure shown in (b) is austenitic/martensitic.
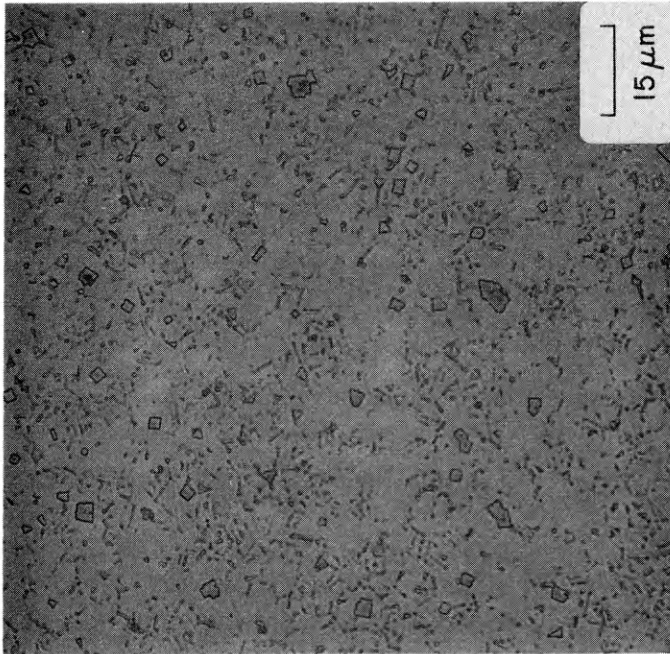
(a) Unetched
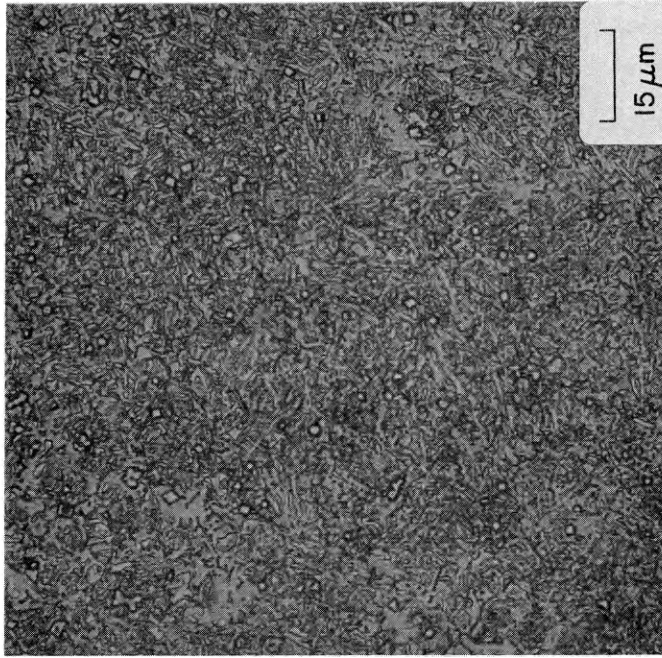
(b) Etched in 2% nital

Figure 28.- Microstructures of alloy 3. The matrix structure revealed in (b) is ferritic.
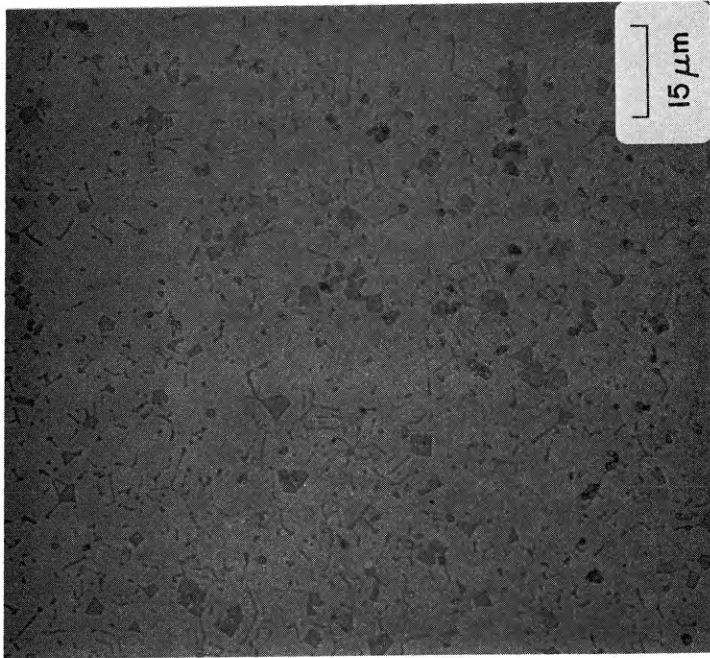
(b) Etched in Villela's Reagent

(a) Unetched
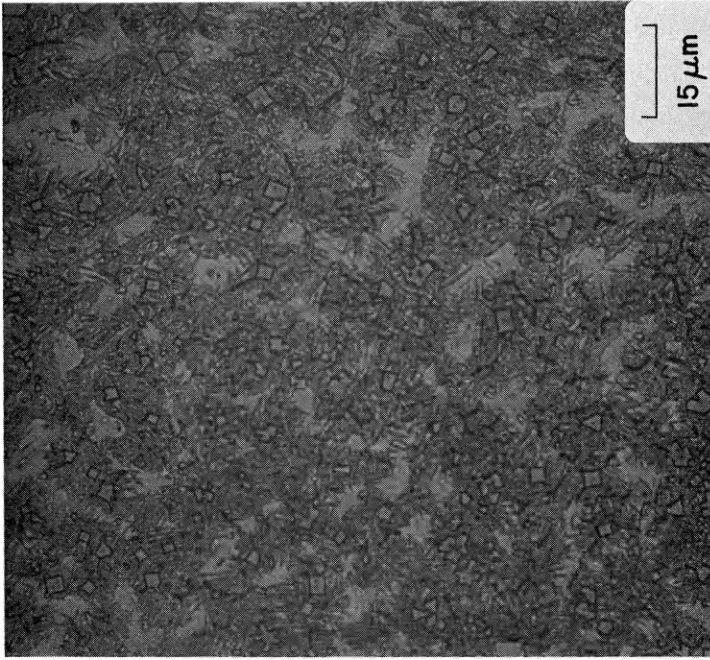
Figure 29.- Microstructure of alloy 4. The matrix structure shown in (b) is austenitic/martensitic.

larger carbide average size (see Table 10 for results from quantitative metallography). In alloy 1, most of the larger TiC particles floated to the top of the weld pool so the average particle was relatively small. The titanium carbides tend to float because of their low specific gravity (4.93) compared to that of the melt (about 7.8). From a force balance of a given spherical particle suspended in a liquid (36), the terminal velocity with which the particle moves towards the top of the liquid weld pool, assuming laminar flow, is given by:

$$V_t = \frac{2R^2 g}{9\eta} (\rho - \rho_p) \qquad (5)$$

where V_t = terminal velocity of particle

R = particle radius

g = acceleration of gravity

η = melt viscosity

ρ = melt density

ρ_p = particle density

Thus, this velocity increases as the radius of the particle squared, meaning that the larger particles will float much faster than the small ones. In alloy 2, the amount of carbides was large enough that some of the large

Table 10

Results From Quantitative Metallography

Alloy	Average Carbide Radius (μm)	Volume % TiC	Mean Free Path (μm)
1	1.6	5.6	36
2	2.2	9.3	29
3	1.7	6.9	30
4	1.6	9.6	17

ones managed to stay in the melt until solidification
occurred; however, most of the large carbides seemed to
float out in alloy 1. Indeed, a small layer of relatively
large carbides was observed on the inside surface of the
solidified slag. The carbide distribution of alloy 3
(Figure 28-a) was similar to that of 1, although the volume
fraction was slightly higher as shown in Table 10. On the
other hand, alloys 2 and 4 had a similar volume fraction of
TiC, except that alloy 2 had larger carbides.

Alloys 1 and 2 were designed to have similar matrix
compositions, so that the only variable changing would be
the size and distribution of the titanium carbides. Figures
26 and 27 show that this was satisfactorily accomplished,
since the matrices appear to be mostly martensitic with some
retained austenite. Note however that alloy 1 was high
enough in chromium and carbon that some ledeburite was
formed, which shows up in Figure 26 as a clear
interdendritic phase $((Fe,Cr)_3C)$ with dark spots of
austenite.

Alloy 3 was designed to have an essentially pure
ferrite matrix so that the effect of a very soft and ductile
matrix on abrasion resistance could be observed. Figure 28

shows that a very fine-grained ferritic matrix was obtained.

Finally, alloy 4 featured a nominal Cr content of 7.5% which was much higher than the 3% contained in alloys 1 and 2. Its matrix appears martensitic/austenitic (Figure 29), with more retained austenite than alloy 2.

3.2.2 Abrasion Test Results

Table 11 is a summary of the abrasion test results, reported as weight losses from the standard ASTM test. Since the density of all the alloys were all very close, these numbers are all proportional to the volume losses, and therefore may be compared to one another. Essentially the same wear behavior was exhibited by all the alloys whose matrix was martensitic, regardless of the carbide volume fraction. Changing the matrix to ferrite (alloy 3) caused the wear to increase in the order of four times as much. It seems then that the matrix does play a role in the abrasion resistance of this type of alloy.

Figures 30 and 31 are SEM micrographs taken looking down at the wear scars from abrasion-test samples of alloys 1 and 3 respectively. While Figure 30 shows a relatively

Table 11

Summary of Abrasion Test Results for Alloys
in Matrix 2. Weight Loss Values are from
the ASTM G-65-80 Dry Sand/Rubber Wheel
Abrasion Test.

Alloy	Weight Loss in Abrasion Test (g)
1	0.26
2	0.25
3	0.92
4	0.26
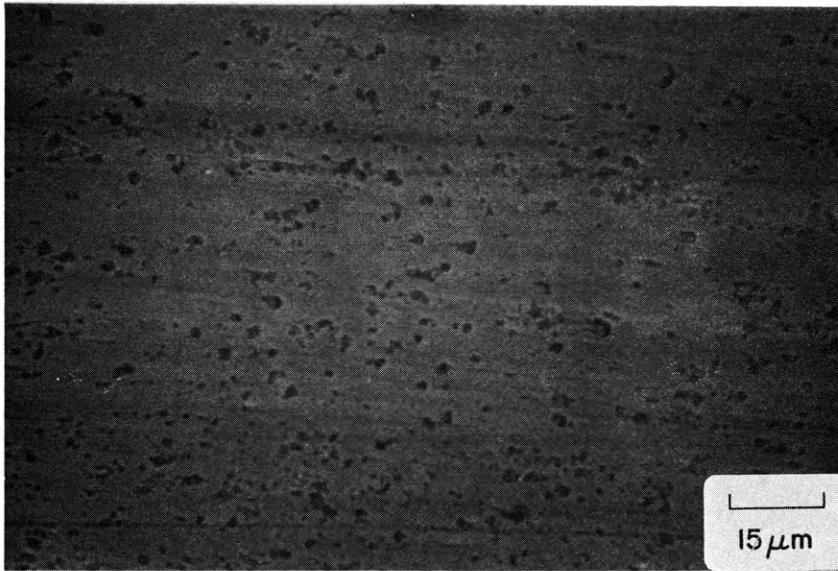
Figure 30.- SEM micrograph of wear scar of
            alloy 1.

Figure 31.- SEM micrograph of wear scar of
            alloy 3.

smooth matrix surface with titanium carbides sticking out of
the surface, Figure 31 shows much more scratch-type scars,
and some parts were material has been removed in small
pieces; also, most of the carbides have been removed from
the ferritic surface, leaving small holes behind.

Thus we see two distinctly different wear mechanisms
which appear to depend on the matrix material. On the hard
matrix of alloy 1, the relatively large abrading particles
seem to mainly slide on top of the titanium carbides, while
very gradually removing matrix material in a preferential
way. The carbides, being very hard, wear down very slow
relatively to the matrix; the wear of the carbides is then
the rate-determining step of the abrasion process. On alloy
3, the soft ferritic matrix is not strong enough to hold on
to the carbides under the action of the abrading particles,
and the result is that the carbides are easily pulled out,
leaving holes behind that show up on the wear scar. As
pointed out by Sare (37), material loss by abrasion is
actually a balance between two rate events: matrix removal
and carbide removal, the overall rate being determined by
the slower of these interdependent processes. If the stress
involved is too low for carbide pullout, carbide wear will
be the rate-limiting mechanism. This is clearly the case in

alloys 1, 2 and 4.

The exact mechanism for carbide removal is not certain; a possible sequence of events is as follows: under the repeated force and bending moment applied by the abrading particles on the carbides, these may plastically deform the ferritic matrix, first opening up a small cavity in the carbide/matrix interface, which will grow to the point where the carbide becomes unattached from the matrix. Another factor possibly involved in the removal of the titanium carbides during abrasion is the bond strength between the carbide and the matrix, but this is probably of secondary importance since both the carbide/ferrite and carbide/martensite interfaces are probably incoherent.

Summarizing, it seems that having a matrix with a lower yield strength will facilitate carbide pullout even when very little of the surrounding matrix has been removed. On the other hand, a hard matrix would have to be substantially removed around a carbide before the latter can be pulled out. In the case of the results from alloy A, a variety of matrix microstructures were produced by changing welding process parameters, but all the wear losses were similar. It seems that in this case all the range of matrices produced

had a yield strength high enough to prevent carbide pullout.
It follows that there must be some threshold level of yield
strength or possibly some other complex parameter below
which the matrix will be ineffective during low-stress
abrasion. More extensive data is needed to determine this
parameter.

The reason why carbide distribution did not seem to
affect the wear loss during the abrasion test may be that,
for the range of distributions studied, the sliding action
of the sand particles over the carbides did not change much,
given the large size of the sand particles compared to the
microstructures tested. Figure 32 shows a typical sand
particle compared to one of the carbide distributions
studied. The large difference in scale suggests that
doubling the average mean free path between the carbides
will still cause the same sliding action, as long as the
stress is low enough to prevent early carbide pullout (see
Figure 33). This situation would probably change if
abrasion occurred at higher stresses where at least some of
the carbides could be pulled out, in which case the wear of
the matrix and its mechanical properties would assume
increasing importance in the overall process.
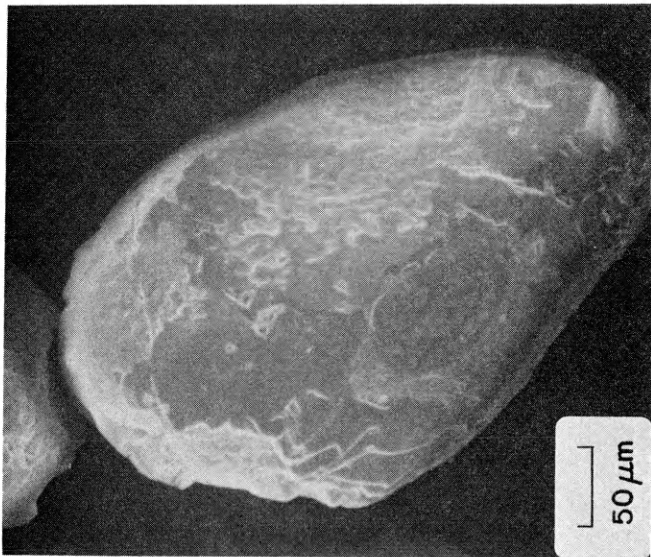
(a) Sand particle
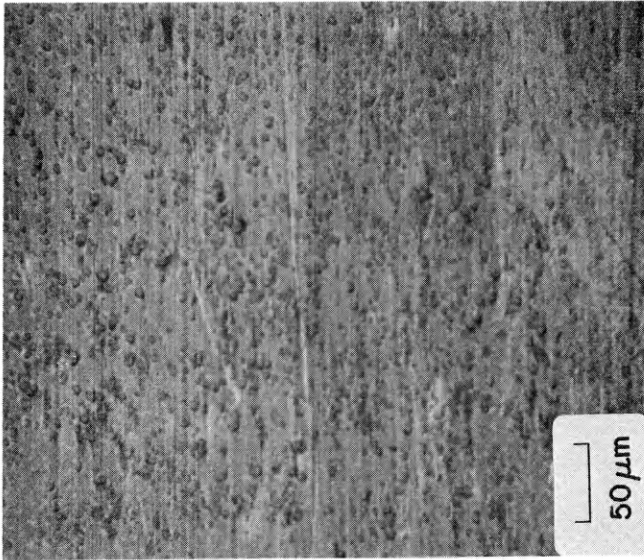
(b) Wear surface of alloy A

Figure 32.- Size of a typical sand particle used in abrasion testing compared to the size and distribution of carbides in alloy A.

No Pullout

λ large

λ small
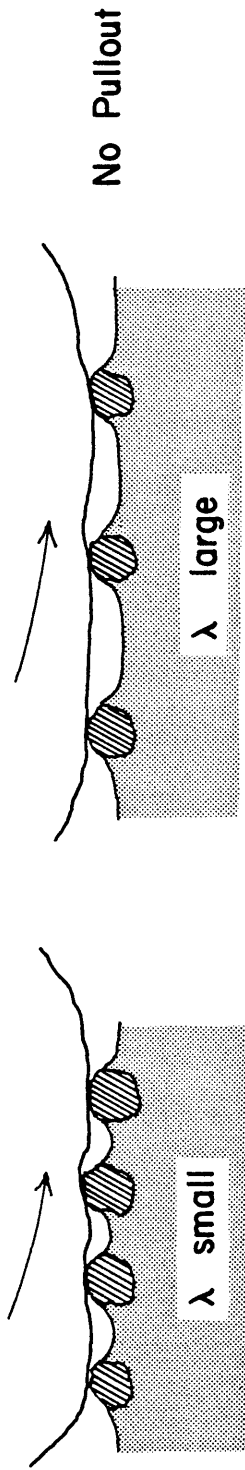
(a) Similar low wear rates

Pullout
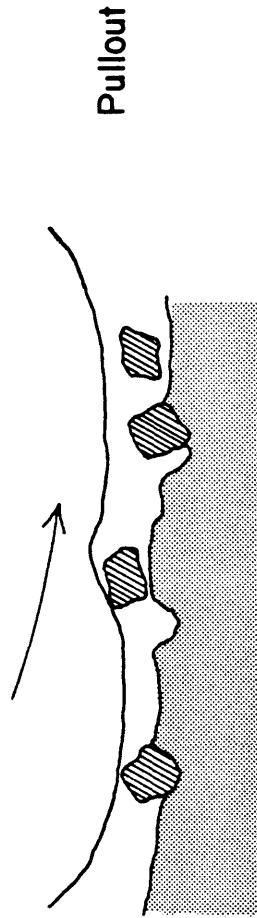
(b) High wear rate

Figure 33.- Schematics of a sand particle sliding on top of a hardfacing deposit containing titanium carbides, showing the two extreme wear mechanisms observed in this study.

CONCLUSIONS

Two systematic studies were conducted on TiC-type hardfacing alloys: the first involved using a single alloy and changing the welding process variables; the second involved using fixed process variables and changing the chemical composition to get different microstructures. The following was concluded:

1. By moving in V-I process space, the matrix microstructure of TiC-type deposits varied considerably, but the carbide volume fraction and distribution remained relatively unaffected because dilution was never large enough to significantly change the mean free path or volume fraction of carbides in the microstructure.

2. Abrasion testing showed that the range of matrix microstructures obtained made no difference on the wear rates obtained.

3. Much larger wear rates were obtained with a ferritic matrix than with an austenitic/martensitic matrix. SEM examination revealed that carbide pullout was probably the dominant mechanism with a soft matrix like ferrite.

4. Similar wear rates were obtained with small and large carbides, and with different volume fractions, all with austenite/martensite matrices. It was rationalized that because all the carbide dispersions studied were so fine compared to the sand particles used for abrasion testing, changing the carbide size and mean free path did not significantly affect the wear mechanism, by which the sand slid on top of the carbides. As long as the matrix was strong enough to hold the carbides in place during the abrasion process, the wear rate did not significantly change.

REFERENCES

1.   Kelley, K.N., "Industry Looks Hard at Hardsurfacing", Welding Design and Fabrication", August 1975, pp. 39-46.

2.   Perrott, C.M. and Powell, G.L.F., "Hardfacing for Wear Resistance", Papers for International Institute of Welding Public Session 1976 and Metals Technology Conference, Sydney, Australia, August 1976, vol. A, Session 6, Paper 2, pp. 6-2-1 to 6-2-18.

3.   Dawson, R.J., Shewchuck, S. and Pritchard, J.E., "Selection and Use of Hardfacing Alloys", Proceedings of the Intermountain Minerals Symposium, Vail, Colorado, August 1982, p. 109.

4.   Metals Handbook, 9th Edition, American Society for Metals, vol. 3, 1980, p. 563.

5.   Peate, S.S. and Gregory, E.N., "Weld Surfacing in Perspective", Weld Surfacing and Hardfacing, The Welding Institute, 1980, pp. 1-3.

6.   Australian Welding Research Association, "Hardfacing", AWRA Technical Note 4, Milsons Point, Australia, September 1974.

7.   Avery, H.S., "Surfacing by Welding for Wear Resistance", Composite Engineering Laminates, A.G.H. Dietz, ed., Cambridge, Mass., MIT Press, 1969, p. 255.

8.   Avery, H.S., "Hard Facing Alloys", ASM Technical Report No. C6-17.3, 1966.

9.   Barr, L.C. and Rogers, C.E., "Hardfacing - Past, Present, Future", Welding Journal, December 1963, pp. 968-974.

10.   Farmer, H.N., "Reducing Wear of Heavy Equipment Through Hardfacing", Repair and Maintenance Welding of Heavy Equipment, AWS Conference Proceedings, 1983.

11.   Moore, M.A., "Abrasive Wear", Fundamentals of Friction and Wear of Materials, Metals Park, American Society for Metals, 1980, pp. 73-118.

12.   Zum Gahr, K.H., "How Microstructure Affects Abrasive Wear Resistance", Metals Progress, September 1979, pp. 46-52.

13.   Richardson, R.C.D., "The Wear of Metals by Relatively Soft Abrasives", Wear, vol. 11, 1968, pp. 245-275.

14.   Richardson, R.C.D., "The Wear of Metals by Hard Abrasives", Wear, vol. 10, 1967, pp. 291-309.

15.   "Abrasive Wear - J965", SAE Information Report, Handbook Supplement, Society of Automotive Engineers, 1966.

16.   Avery, H.S., "Work Hardening in Relation to Abrasion Resistance", Materials for the Mining Industry Symposium, Climax Molybdenum Company, 1974, pp. 43-77.

17.   Avery, H.S., "The Measurement of Wear Resistance", Wear, vol. 4, no. 6, 1961, pp. 427-449.

18.   Annual ASTM Standards, "Standard Practice for Conducting Dry Sand/Rubber Wheel Abrasion Tests", Standard G-65-80, Metals - Physical, Mechanical, Corrosion Testing, vol 10, 1980, p. 1044.

19.   Borik, F., "Using Tests to Define the Influence of Metallurgical Variables on Abrasion", Metals Engineering Quarterly, May 1972.

20.   Fairhurst, W. and Rohrig, K., "Abrasion-resistant High-chromium White Cast Irons", Foundry Trade Journal, May 1974.

21.   Griffing, N.R., Forgeng, W.D. and Healy, G.W., "C-Cr-Fe Liquidus Surface", Transactions of the Metallurgical Society of AIME, vol. 224, February 1962, pp. 148-159.

22.   Metals Handbook, Ninth Edition, Volume 3, American Society for Metals, 1980, pp. 563-567.

23.   Nakajima, M., Akira, N., Kusano, T. and Ueda, M., "A Study on a New Hardfacing Process Using an Extremely Hard Material", Mitsubishi Heavy Industries Technical Review", vol. 19, no. 1, February 1982, pp. 9-16.

24.   Aufderhaar, B., "Now Available: TiC Wear Surfacing Powders", Metals Progress, June 1981, pp.30-33.

25. Richardson, F.D., Physical Chemistry of Melts in Metallurgy, Volume 2, London, Academic Press, 1974, p. 344.

26. "Welding Method and Electrode", United States Patent No. 3,231,709, Patented Jan. 25, 1966.

27. Sereda, N.N., Koval'chenko, M.S., Belik, I.T., Solomenko, V.G., Uvarov, V.V. and Fedoseev, V.V., "Use of Hard Alloys Based on Titanium Carbide as Wear-Resistant Materials and Cutting Tools", Poroshkovaya Metallurgiya, vol. 173, no. 5, May 1977, pp.94-97.

28. Mal, M.K. and Tarkan, S.E., "Wear Resistant Steel Bonded Carbides", Wear of Materials 1977, W.A. Glaeser, K.C. Ludema and S.K. Rhee, eds., 1977.

29. Kalish, H.S., "Coatings for Carbide: TiC or TiN?", American Machinist, August 1977, pp. 90-92.

30. Bonetti, R., "Hard Coatings for Improved Tool Life", Metal Progress, June 1981, pp. 44-47.

31. Rense, C.E.C., "The Effect of Process Variables on the Microstructure and Low Stress Abrasion Resistance of Open Arc Chromium Carbide Type Hardfacing Deposits", Master of Science Thesis No. T-2663, Colorado School of Mines, June 1983.

32. Jaramillo, J., "Use of Metal Powders for Manufacturing Consumable Electrodes of Special Alloys", Master of Science Thesis, in progress, Colorado School of Mines, 1983.

33. Maratray, F. and Usseglio-Nanot, R., "Atlas - Transformation Characteristics of Chromium and Chromium-Molybdenum White Irons", Paris, Climax Molybdenum S.A., 1971.

34. Underwood, E.E., "Applications of Quantitative Metallography", Metals Handbook, Eigth Edition, Volume 8, American Society for Metals, 1973, pp. 37-47.

35. Rostoker, W. and Dvorak, J.R., Interpretation of Metallographic Structures, New York, Academic Press, 1977, p. 226.

36. Geiger, G.H. and Poirier, D.R., Transport Phenomena in Metallurgy", Massachusetts, Addison-Wesley, 1980, pp. 70-71.

37. Sare, I.R., "Abrasion Resistance and Fracture Toughness of White Cast Irons", Metals Technology, November 1978, pp. 412-419.

APPENDIX I

CALCULATION OF POWDER COMPOSITIONS FOR THE CORE OF

EXPERIMENTAL ALLOY WIRES

VOLUME FRACTIONS OF TITANIUM CARBIDE

Three alloys were manufactured. The desired TiC volume
fractions in the final deposits were:

Alloy	vol % TiC
1	5
2	20	(Table T1)
3	10

Corresponding weight fractions were calculated from:

$$\text{Wt.\% TiC} = \frac{(\text{vol.\% TiC})(\rho_{TiC})}{(100 - \text{vol.\% TiC})(\rho_{matrix}) + (\text{vol.\% TiC})(\rho_{TiC})} \qquad (A1)$$

The weight percents are then:

Alloy	Wt.% TiC	Wt.% Matrix
1	3.18	96.82
2	13.50	86.50	(Table T2)
3	6.48	93.52

The above numbers are the desired compositions of the final

deposits. However, since the goal here is to calculate the compositions of the consumables, dilution with the base plate must be accounted for. Assuming 30% dilution, the composition of the consumables are:

$$\text{Alloy 1 :} \left(\frac{100}{70}\right) \times 5 \quad = 7.14 \text{ vol.\% TiC}$$

$$\text{Alloy 2 :} \left(\frac{100}{70}\right) \times 20 \quad = 28.57 \text{ vol.\% TiC}$$

$$\text{Alloy 3 :} \left(\frac{100}{70}\right) \times 10 \quad = 14.29 \text{ vol.\% TiC}$$

The corresponding weight percentages for the consumables are:

Alloy	Wt.% TiC	Wt.% Matrix	
1	4.58	95.42	
2	19.97	80.03	(Table T3)
3	9.42	90.58	

CALCULATION OF BULK WIRE COMPOSITIONS

As mentioned in the Experimental Procedure chapter, alloys 1 and 2 were designed to have an austenitic/martensitic matrix, and alloy 3 a ferritic matrix. Since the TiC carbides are introduced solid from the core of the wire, the chemical composition of the matrix may be assumed independent from these carbides.

To achieve an austenitic/martensitic matrix in alloys 1 and 2, the following matrix composition (by weight) was chosen for the beads:

Cr – 3%
C   – 2.5%
Mn – 1.4%
Fe – balance

For alloy 3, the matrix composition was designed to be basically the same than that of 1008 steel, the capsule material:

C   – 0.08%
Mn – 0.4%

Calculation of Undiluted Matrix Composition

Assuming 30% dilution again, the undiluted weight fraction of any matrix alloying element is given by:

$$\% A_{undiluted} = \frac{10(\rho_{bead})(\% A_{bead}) - 3(\rho_{base})(\% A_{base})}{7 \, \rho_{undiluted}}$$

where A is any alloying element and   represents density. Assuming all densities are close enough:

$$\% A_{undiluted} \cong \frac{10(\% A_{bead}) - 3(\% A_{base})}{7} \qquad (A2)$$

The undiluted matrix compositions for alloys 1 and 2 are
calculated from equation A2:

Alloying Element	% in Bead	% in Base (1020 steel)	Undiluted Matrix Percentage	
Cr	3.0	0.04	4.27	
C	2.5	0.20	3.49	(Table T4)
Mn	1.4	0.50	1.79	

For the ferritic matrix of alloy 3:

Alloying Element	% in Bead	% in Base (1020 steel)	Undiluted Matrix Percentage	
Cr	--	0.04	--	
C	0.08	0.20	0.03	(Table T5)
Mn	0.40	0.50	0.36	

To convert the matrix compositions to total bulk
compositions, the former must be multiplied by the weight
percent corresponding to the matrix, obtained from table T3.

The next step is to assume the following estimated
losses for each component during welding:

$$Cr - 1\%$$
$$C \ - 0.3\%$$
$$Mn - 0.4\%$$
$$TiC - none$$

Due to the low alloy content of the matrix of alloy 3, no
losses will be considered in that case. By adding the

losses to the compositions of alloys 1 and 2, the final

undiluted weight compositions of the three wires are

obtained:

Alloy	%Cr	%C	%Mn	%TiC	%Fe	
1	5.07	3.63	2.11	4.58	84.61	
2	4.42	3.09	1.83	19.97	70.69	(Table T6)
3	--	0.03	0.36	9.42	90.20	

These are the bulk compositions of the wires. Now we need

to calculate the powder compositions.

CALCULATION OF POWDER COMPOSITIONS

For the capsule geometry shown in Figure 5:

Volume of steel ring $= \frac{\pi}{4} (2.25)^2(6.0) - \frac{\pi}{4} (1.27)^2(6.0)$

$$= 16.26 \text{ cm}^3$$

Volume of cavity $= \frac{\pi}{4} (12.7)^2(6.0)$

$$= 7.60 \text{ cm}^3$$

Assuming 20 vol.% porosity after compaction:

Net cavity volume $= (7.60)(0.80) = 6.08 \text{ cm}^3$

To calculate the volume fraction of each component in the

powder, we do mass balances.

Let: X_A = weight fraction of component A in powder

   ρ_A = density of component A

   $\bar{\rho}$ = average powder density

   ρ_{alloy} = density of undiluted alloy

   %A = weight percentage of component A in undiluted alloy

1. $X_{Fe} + X_{Cr} + X_C + X_{Mn} + X_{TiC} = 1$ \hfill (1)

2. $C_{shell} + C_{powder} = $ Total C

   $(16.26)(0.008)\rho_C + (6.08)\bar{\rho}X_C = \dfrac{1}{100}(16.26 + 6.08)\rho_{alloy}$ (%C)

   $(0.013)\rho_C + (6.08)\bar{\rho}X_C = 0.2234$ (%C)ρ_{alloy} \hfill (2)

3. $Cr_{shell} + Cr_{powder} = $ Total Cr

   $(6.08)\bar{\rho}X_{Cr} = 0.2234$ (%Cr)ρ_{alloy} \hfill (3)

4. $Mn_{shell} + Mn_{powder} = $ Total Mn

   $(0.065)\rho_{Mn} + (6.08)\bar{\rho}X_{Mn} = 0.2234$ (%Cr)ρ_{alloy} \hfill (4)

5. $Fe_{shell} + Fe_{powder} = $ Total Fe

   $(16.26)\rho_{Fe} + (6.08)\bar{\rho}X_{Fe} = 0.2234$ (%Fe)ρ_{alloy} \hfill (5)

6. $TiC_{shell} + TiC_{powder} = Total\ TiC$

$$(6.08)\bar{\rho}X_{TiC} = 0.2234\ (\%TiC)\rho_{alloy} \tag{6}$$

7. $\dfrac{\%Fe}{\rho_{Fe}} + \dfrac{\%Cr}{\rho_{Cr}} + \dfrac{\%C}{\rho_C} + \dfrac{\%Mn}{\rho_{Mn}} + \dfrac{\%TiC}{\rho_{TiC}} = \dfrac{100}{\rho_{alloy}} \tag{7}$

These equations were solved by the computer program program showed in Appendix II, giving the following powder compositions:

Alloy	%Cr	%C	%Mn	%Fe	%TiC	
1	26.4	18.79	9.40	21.52	23.84	
2	15.3	10.62	5.21	--	69.13	(Table T7)
3	--	0.26	0.48	57.75	41.5	

APPENDIX 2

COMPUTER PROGRAM TO CALCULATE POWDER COMPOSITIONS FROM

OVERALL WEIGHT COMPOSITIONS

```
100 PRINT"Enter percent compositions of Cr, C, Mn, Fe, TiC for alloy desired"
110 INPUT C1,C2,C3,C4,C5
120 PRINT"Enter initial value for x(Cr)"
130 INPUT X1
140 PRINT"Enter increment for x(Cr)"
150 INPUT I
160 B=0
165 P=100/(C1/7.2+C2/2.62+C3/7.43+C4/7.86+C5/4.93)
170 PRINT
180 LPRINT"x1","x2","x3","x4","x5","sum"
190 LPRINT
200 X1=X1+I
205 D=.2234*P*C1/X1/6.08
210 X2=(.2234*P*C2-.013*2.62)/6.08/D
220 X3=(.2234*P*C3-6.500001E-02*7.43)/6.08/D
230 X4=(.2234*P*C4-16.26*7.86)/6.08/D
235 IF X4<0 THEN X4=0
240 X5=.2234*P*C5/6.08/D
250 S=X1+X2+X3+X4+X5
260 LPRINT X1,X2,X3,X4,X5,S
270 PRINT
280 IF ABS(ABS(S)-1)<.001 THEN 320
300 IF S<1 THEN 200
310 I=-I
320 K1=X1*100
330 K2=X2*100
340 K3=X3*100
345 K4=X4*100
350 K5=X5*100
360 REM ***** printing statements ****************
370 PRINT
380 PRINT
390 LPRINT"Alloy Composition: ";C1;" %Cr ";C2;" %C ";C3;" %Mn ";C4;" %Fe ";
400 LPRINT C5;" %TiC"
405 LPRINT
410 LPRINT"Powder Composition:"
415 LPRINT
420 LPRINT,K1;" %Cr"
430 LPRINT,K2;" %C"
440 LPRINT,K3;" %Mn"
450 LPRINT,K4;" %Fe"
460 LPRINT,K5;" %TiC"
470 END
```